

Title

Neuronal coupling by endogenous electric fields: Cable theory and applications to coincidence detector neurons in the auditory brainstem

Authors

Joshua H. Goldwyn^{1,2,3}

John Rinzel^{1,2}

Contributions

JHG and JR designed study, analyzed data, and wrote manuscript. JHG performed simulations.

Affiliations

¹ Center for Neural Science, New York University, New York, NY, United States

² Courant Institute of Mathematical Sciences, New York University, New York, NY, United States

³ Department of Mathematics, Ohio State University, Columbus, OH, United States

Running Head

Neuronal coupling by endogenous electric fields

Address for Correspondence

Joshua H. Goldwyn

100 Math Tower

231 West 18th Avenue

Columbus OH, 43210-1174

Phone: 614-292-5256

Fax: 614 292-1479

Email: jhgoldwyn@gmail.com

Abstract

The ongoing activity of neurons generates a spatially- and time-varying field of extracellular voltage (V_e). This V_e field reflects population-level neural activity, but does it modulate neural dynamics and the function of neural circuits? We provide a cable theory framework to study how a bundle of model neurons generates V_e and how this V_e feeds back and influences membrane potential (V_m). We find that these “ephaptic interactions” are small but not negligible. The model neural population can generate V_e with millivolt-scale amplitude and this V_e perturbs the V_m of “nearby” cables and effectively increases their electrotonic length. After using passive cable theory to systematically study ephaptic coupling, we explore a test case: the medial superior olive (MSO) in the auditory brainstem. The MSO is a possible locus of ephaptic interactions: sounds evoke large V_e *in vivo* in this nucleus (millivolt-scale). The V_e response is thought to be generated by MSO neurons that perform a known neuronal computation with submillisecond temporal precision (coincidence detection to encode sound source location). Using a biophysically-based model of MSO neurons, we find millivolt-scale ephaptic interactions consistent with the passive cable theory results. These subtle membrane potential perturbations induce changes in spike initiation threshold, spike time synchrony, and time difference sensitivity. These results suggest that ephaptic coupling may influence MSO function.

Keywords

Ephaptic coupling, medial superior olive, cable theory, extracellular voltage, coincidence detection

INTRODUCTION

Neurons are bathed in a shared extracellular voltage (V_e) that is generated by voltage-gated ionic currents, synaptic currents, and other transmembrane currents (see Buzsáki et al. 2012 for review). This endogenous V_e can be recorded *in vivo* using depth electrodes (e.g. the local field potential) and is detectable on the surface of the scalp (e.g. electroencephalography). It has long been known that applied (i.e. “exogenous”) V_e , delivered via a stimulating electrode, can evoke and modulate neural activity (Strumwasser and Rosenthal 1960, e.g.). Indeed, this is the basic mechanism by which neural prostheses such as cochlear implants and deep brain stimulation provide therapeutic benefits. The functional consequences of endogenous V_e , however, remain a subject of investigation. In this work, we present an idealized model for assessing neuronal coupling via endogenous V_e . We develop a cable theoretic framework that shows how millivolt-scale endogenous V_e can induce millivolt-scale perturbations in membrane potential. We apply these insights to the medial superior olive in the auditory brainstem and find (in simulations) that ephaptic coupling can alter spike activity in these specialized coincidence detector neurons.

Following Arvanitaki (1942), we refer to interactions between neurons mediated by endogenous extracellular voltage as *ephaptic* interactions. She had “no doubt that the activity of an element in the midst of a cell agglomeration can influence that of its neighbors [via ephaptic coupling]” (Arvanitaki 1942). Classical studies of interactions between side-by-side axons supported her assertion (Katz and Schmitt 1940; Arvanitaki 1942; Ramón and Moore 1978) and recent studies have demonstrated that relatively weak and oscillatory applied V_e (designed to be “endogenous-like”) can enhance spike time synchrony *in vitro* (Radman et al. 2007; Frölich and McCormick 2010; Anastassiou et al. 2011).

In this work, we present a systematic study of ephaptic coupling in a bundle of dendrites using methods that are an extension of classical cable theory (Rall 1977). By invoking assumptions of cable theory and by considering a population of identical neurons (see Materials and Methods), we solve the ephaptic coupling problem by computing intra- and extracellular voltages in coupled one-dimensional domains. This approach differs from standard “line-source” or “point-source” approximations in which V_e is computed from simulated neural activity without including any feedback between V_e and neural activity (Klee and Rall 1977; Holt and Koch 1999; Lindén et al. 2011; Reimann et al. 2013). Our method is substantially simplified compared to solvers that couple membrane dynamics of three-dimensional neuron models to Maxwell’s equations for extracellular electric and magnetic fields (Malik 2011; Agudelo-Toro and Neef 2013).

We consider a population of identical model neurons that receive identical inputs and that are arranged with spatial symmetry (i.e. equally spaced and oriented parallel to one another). These assumptions appear restrictive, but the approach is inspired by pioneering analyses of endogenous V_e in the olfactory bulb (Rall and Shepherd 1968) and cerebellum (Nicholson and Llinás 1971). We have found this idealized modeling approach useful to describe sound-evoked extracellular voltages recorded *in vivo* in the auditory brainstem (Goldwyn et al. 2014).

The auditory brainstem V_e is an intriguing test case for studying ephaptic interactions. Neurons in the medial superior olive (MSO) are believed to generate the auditory brainstem V_e (Galambos et al. 1959; Biedenbach and Freeman 1964; Moushegian et al. 1964; Tsuchitani and Boudreau 1964; Clark and Dunlop 1968; Mc Laughlin et al. 2010; Goldwyn et al. 2014). The dense packing of MSO neurons' dendrites and the presence of a prominent, sound-evoked extracellular voltage field have led to suggestions that ephaptic interactions may be at work in this nucleus (Schwartz 1977; Ashida and Carr 2011). MSO neurons perform a known computation: sound localization via temporally precise coincidence detection of dendritic inputs (see Grothe et al. 2010 for review). We can evaluate the functional consequences of ephaptic interactions in this system by simulating coincidence detection in MSO neuron models in the presence of (simulated) endogenous V_e .

MSO neurons are bipolar (two dendrites with modest branching, extending away from a central soma, Rautenberg et al. 2009). Back-propagating action potentials in the soma are small (Scott et al. 2007; Franken et al. 2015) and are difficult to detect with extracellular and juxtacellular electrodes (Yin and Chan 1990; van der Heijden et al. 2013). It is reasonable, therefore, to begin our study with a passive cable model and neglect contributions of spike-generating Na currents. In this initial analysis we gain insights into ephaptic interactions in the MSO and dendritic bundles in general. We find that the cable population can generate millivolt-scale V_e and that this V_e can induce a millivolt-scale perturbation in the membrane potential of a neuron embedded in the V_e bath. These ephaptic interactions are largest for electrotonically compact cables (i.e. large cable space constant).

The passive cable results illustrate that V_e , due to its spatially-distributed nature, can hyperpolarize or depolarize different portions of a “nearby” neuron. As a corollary, when we extend our MSO neuron model to include spike-generating Na currents, we find that ephaptic coupling can have either “excitatory” or “inhibitory” effects depending on the location of spike initiation in the spatially-varying V_e . The relatively modest (millivolt-scale) perturbations of membrane potential due to endogenous V_e alter spike initiation threshold, spike timing, and the sensitivity of MSO neurons to arrival times of bilateral inputs. Specifically, we find that ephaptic coupling suppresses spiking activity if spikes are generated near the soma of the MSO neuron model and promotes spiking activity if spikes are generated at locations distant from the soma. Our results establish, in principle, that ephaptic coupling can influence neural processing in this early stage of the auditory pathway.

Glossary

General

t	Time [ms]
x	Distance [cm]
V_i	Intracellular voltage [mV]
V_e	Extracellular voltage [mV]
$V_m = V_i - V_e$	Transmembrane potential [mV]

E_{lk}	Reversal potential of leak current [mV]
r_i	Intracellular (core) resistance per unit length [Ω/cm]
r_e	Extracellular resistance across per unit length [Ω/cm]
N	Number of neurons in population
$\kappa = Nr_e/r_i$	Coupling constant
$\rho = R_e/R_i$	Resistivity ratio
δ	Packing density
A_i, A_e	Cross-sectional area of intra- and extracellular domains [cm^2]
\wedge	Parameter or variable associated with “test” neuron (I_m^* , e.g.)

Passive cable model

c_m	Capacity per unit length [mF/cm]
r_m	Resistance across a unit length [Ωcm]
$\tau = c_m r_m$	Membrane time constant [ms]
$\lambda = \sqrt{r_m/r_i}$	Cable space constant [cm]
λ_{ref}	“Reference value” of cable space constant [cm]
$T = t/\tau$	Nondimensional time variable
$X = x/\lambda$	Nondimensional space variable
$L = l/\lambda$	Nondimensional length of cable
i_{in}	Input current per unit length [mA/cm]
i_m	Membrane current per unit length [mA/cm]
l	Physical length of cable [cm]
d_g	Distance from end of cable to electric ground [cm]
ω	Frequency of sinusoidal current input (Hz)
U_m, U_i, U_e	Voltage in Fourier domain

Medial superior olive model

C_m	Capacitance [mF/cm ²]
R_i	Intracellular (axial) resistivity [Ωcm]
R_e	Extracellular resistivity [Ωcm]
I_i, I_e, I_m, I_{in}	Intracellular, extracellular, transmembrane, and input current [mA]
J_{in}	Input current density [mA/cm ²]
$G_{lk}, G_{KLT}, G_h, G_{Na}$	Maximal conductance density for leak, KLT, h, and Na currents [mS/cm ²]
E_K, E_h, E_{Na}	Reversal potential for K, h and Na currents [mV]
w, z	Gating variables for KLT current
m, h	Gating variables for Na current
u_∞	Steady-state functions for gating variables [where $u = w, z, m, \text{ or } h$]
τ_u	Time constants for activation and inactivation variables [where $u = w, z, m, \text{ or } h$]
G_{syn}	Maximal synaptic conductance density [mS/cm ²]
E_{syn}	Reversal potential of synaptic current [mV]

τ_{syn}	Synaptic conductance time constant [ms]
t_0	Onset time of synaptic event [ms]
g_{axial}	Axial conductance between soma and spike initiation zone [nS]
d	Diameter of MSO neuron model [cm]
Δx	Length of compartment in discretized MSO neuron model [cm]
S	Surface area of compartment [cm ²]

MATERIALS AND METHODS

Ephaptic coupling in a population of passive cables

Model Formulation: In the standard (passive) cable theory, spatio-temporal dynamics of membrane voltage $V_m(x,t)$ are governed by the balance of capacitative, leak, and applied currents crossing the cell membrane and diffusion of current within the cell (Rall 1977):

$$c_m \frac{\partial V_m}{\partial t} = -\frac{1}{r_m} (V_m - E_{lk}) + \frac{1}{r_i} \frac{\partial^2 V_i}{\partial x^2} + i_{in}. \quad (1)$$

c_m is the membrane capacity per unit length [mF/cm], r_m is the resistance across a unit length of membrane [Ω cm], r_i is intracellular (core) resistance per unit length [Ω /cm], E_{lk} is the leak current reversal potential [mV], and i_{in} is input current per unit length [mA/cm]. At the ends of the cable, we impose a “sealed-end” (zero axial current) boundary condition by requiring $\partial V_i / \partial x = 0$ for $x = 0$ or l where l is the physical length of the cable. In all cable model simulations, we will present V_m as its deviation from resting potential (or, equivalently, set $E_{lk} = 0$ mV).

To gauge the effect of V_e on V_m , one can substitute $V_m + V_e$ for V_i in Eq. 1:

$$c_m \frac{\partial V_m}{\partial t} = -\frac{1}{r_m} (V_m - E_{lk}) + \frac{1}{r_i} \frac{\partial^2 V_m}{\partial x^2} + \frac{1}{r_i} \frac{\partial^2 V_e}{\partial x^2} + i_{in}. \quad (2)$$

In this formulation, the effect of V_e on the dynamics of V_m appears as a spatially distributed current source proportional to the second spatial derivative of V_e . Positive curvature of V_e acts locally as a depolarizing (“excitatory”) current. This is the basis for the *activating function* method (Rattay 1986), a heuristic used to approximate the effect of applied extracellular fields on neurons, for instance in studies of neural prostheses (Rattay 1999). Holt and Koch (1999) refer to the second spatial derivative of V_e divided by r_i as a “fictitious distributed current (the ephaptic current).”

A common modeling assumption is that extracellular voltage has a negligible impact on the cell’s voltage dynamics. In that case, since $V_m = V_i - V_e$, one sets $V_e = 0$ for all x (no “ephaptic current”) and lets $V_i = V_m$. We are specifically investigating how V_e affects neuronal dynamics via ephaptic interactions so we retain V_i in Eq. 1 as a quantity distinct from V_m .

We now describe how the activity of neurons generates V_e and how this V_e feeds back and influences V_m in an idealized model of N identical and parallel cables. If all such cables receive similar input i_{in} (in terms of temporal dynamics and spatial

location), then the spatio-temporal distribution of membrane currents will be similar across the population. As a consequence, V_e in the region surrounding any one cable will be similar to V_e surrounding any neighboring cable in the population. In other words, the gradient of V_e (which is proportional to the current flow in the extracellular region) will be directed, for the most part, parallel to the orientation of the cables. We thus make the assumption that the extracellular space can be described as one-dimensional volume conductor. This reduces the problem of modeling extracellular interactions to two, coupled one-dimensional domains: the inside of the cable (intracellular core conductor) and a thin layer surrounding the cable (extracellular volume conductor).

In the one-dimensional extracellular region, there is a current balance relationship comprised of the sum of all membrane currents in the population of N cables $i_m = \sum_{n=1}^N \left[c_m \frac{\partial V_m^{(n)}}{\partial t} + \frac{1}{r_m} (V_m^{(n)} - E_{ik}) - i_{in}^{(n)} \right]$ and current flow along the one-dimensional extracellular pathway $-\frac{1}{r_e} \frac{\partial^2 V_e}{\partial x^2}$, where r_e is the resistance per unit length [Ω/cm] in the extracellular region in the direction parallel to the cables. The superscript (n) is the index of neurons in the population. Under the assumption described above, $i_{in}^{(n)}$ (and, therefore, $V_m^{(n)}$) are similar for all N cables, so we divide by N and obtain the population-averaged current balance relation

$$c_m \frac{\partial V_m}{\partial t} = -\frac{1}{r_m} (V_m - E_{ik}) - \frac{1}{Nr_e} \frac{\partial^2 V_e}{\partial x^2} + i_m. \quad (3)$$

V_m and i_m represent population-averaged quantities, for instance $V_m = \frac{1}{N} \sum_{n=1}^N V_m^{(n)}$. Note that the intracellular current balance relation in Eq. 1 still holds if V_m , V_i , and i_m are population-averaged quantities, so going forward we will maintain this mean-field perspective. A more general formulation would allow the applied current i_m to differ in the intracellular and extracellular domains (cf. Tuckwell 1988). We consider i_m to be transmembrane current (synaptic current, for example) so we require the applied intra- and extracellular currents to be identical.

Extracellular space extends beyond the ends of the cables and volume conduction allows V_e to spread to a distant electric ground at which $V_e = 0$ mV. We impose a mixed boundary condition that describes the flow of current to electric ground along a one-dimensional current pathway of length d_g . These boundary conditions are $d_g \partial V_e / \partial x - V_e = 0$ at $x = 0$ and $d_g \partial V_e / \partial x + V_e = 0$ at $x = l$.

Using a standard re-parameterization, we define the time and space constants of the cable (Rall 1977): $\tau = c_m r_m$ and $\lambda^2 = r_m / r_e$. In addition, we introduce a coupling parameter $\kappa = Nr_e / r_e$. The governing equations for the coupled, intracellular/extracellular system are:

$$\tau \frac{\partial V_m}{\partial t} = -(V_m - E_{ik}) + \lambda^2 \frac{\partial^2 V_e}{\partial x^2} + r_m i_m. \quad (4)$$

$$\tau \frac{\partial V_{in}}{\partial t} = -(V_m - E_{ik}) - \frac{\lambda^2}{\kappa} \frac{\partial^2 V_e}{\partial x^2} + \tau_m i_{in}. \quad (5)$$

$$\frac{\partial V_i(x, t)}{\partial x} \Big|_{x=0, l} = 0 \quad (6)$$

$$d_g \frac{\partial V_e(0, t)}{\partial x} - V_e(0, t) = 0 \text{ and } d_g \frac{\partial V_e(l, t)}{\partial x} + V_e(l, t) = 0 \quad (7)$$

We will often report results in terms of the nondimensional spatial variable $X = x/\lambda$ and the cable length $L = x/\lambda$.

To further investigate ephaptic coupling, we embed an additional neuron, with possibly different cable properties and input current, into the surrounding V_e . We ignore its $O(1/M)$ contribution to V_e and the population-averaged V_m , but since membrane potential is the difference between intracellular and extracellular voltage, V_e perturbs this additional neuron's membrane potential. We refer to this as a "test neuron" and its membrane and intracellular voltages satisfy Eq. 4 and the boundary condition in Eq. 6. We use the ^ accent to indicate parameter values for the test neuron that differ from the cable population. We note that there is no spike generating mechanism in the passive cable model. We view this as a subthreshold model and are neglecting any contributions of spiking activity to V_e and ephaptic interactions.

Solution Method: Equations 4-7 form a system of partial differential algebraic equations (PDAEs) and, in general, require special solution methods (Lucht et al 1997a, 1997b). For simple cases (constant or sinusoidal input current i_{in} injected at a single point on the cable), we reformulate and solve these equations numerically as a boundary value problem. For general current waveforms (and voltage-gated membrane currents), numerical solution methods are available to integrate these equations in time (see solution method for MSO model, below).

In response to a constant current input, the system will reach a steady state with $\partial V_m/\partial t = 0$. This eliminates the time dependence in Eqs. 4 and 5. Steady state spatial profiles of V_i and V_m satisfy a linear, constant coefficient system of ordinary differential equations:

$$\lambda^2 V_i'' = V_i - V_e - E_{ik} - \tau_m i_{in} \quad (8)$$

$$\frac{\lambda^2}{\kappa} V_e'' = -(V_i - V_e - E_{ik}) + \tau_m i_{in} \quad (9)$$

$$\lambda^2 \mathcal{V}_i'' = \mathcal{V}_i - V_e - E_{ik} - \tau_m i_{in} \quad (10)$$

with boundary conditions given in Eqs. 6 and 7. Derivatives in these equations are with respect to the spatial variable x and the ^ accent indicates parameters and variables associated with the test neuron. We solve this boundary value problem using the function `bvp4c` in MATLAB (R2012b, The MathWorks Inc.).

We can also formulate a boundary value problem to describe the frequency-response characteristics of the coupled intracellular-extracellular system. In response to the stimulus $i_{in} = i_o \exp(i2\pi\omega t) \delta(x-x_o)$, intracellular and extracellular voltages are of the form $V_i(x) = U_i(x)\exp(i2\pi\omega t) + E_{lk}$ and $V_e(x) = U_e(x)\exp(i2\pi\omega t)$ and solve the following ordinary differential equations:

$$\lambda^2 U_i'' = (1 + i2\pi\tau\omega)(U_i - U_e) - r_m i_o \delta(x - x_o) \quad (11)$$

$$\frac{\lambda^2}{\kappa} U_e'' = -(1 + i2\pi\tau\omega)(U_i - U_e) + r_m i_o \delta(x - x_o) \quad (12)$$

$$\lambda^2 U_i'' = (1 + i2\pi\tau\omega)(U_i - U_e) - r_m i_o \delta(x - x_o). \quad (13)$$

The boundary conditions in Eqs. 6 and 7 are applied to the amplitude variables $U(x)$ and we solve these equations using `bvp4c` in MATLAB. We report the amplitude of the oscillatory response to i_{in} as the absolute value of $U(x)$ and use the `phase` command in MATLAB to recover the phase of the response. Note that the intracellular amplitude U_i measures the deviation of the intracellular voltage from the resting potential E_{lk} . In all simulations, we will present cable model V_m responses in terms of their deviation from rest (equivalent to setting $E_{lk} = 0$ mV in above equations).

Ephaptic coupling in an idealized model of the medial superior olive

Model formulation: Neurons of the MSO are thought to generate prominent extracellular voltages in response to acoustic stimuli (Galambos et al. 1959, e.g.). In previous work, we developed an MSO model that predicted spatiotemporal features of these extracellular voltage responses (Goldwyn et al. 2014). Here, we adapt this model to test ephaptic interactions among MSO neurons. The MSO neuron model differs from the passive cable discussed above because it includes voltage-gated membrane current in addition to the leak current and a non-uniform morphology (two dendrites, connected to a soma). These nonlinearities and inhomogeneities interfere with the construction of a population-averaged model.

However, we have argued previously that a mean-field perspective is justified for describing *in vivo* MSO responses to pure tone stimuli (Goldwyn et al. 2014). Specifically, we noted that MSO neurons have a relatively simple morphology (bipolar dendrites with minimal branching) and are oriented roughly in parallel. Moreover, early stages of the auditory pathway are specialized to deliver inputs to MSO neurons with high levels of phase locking (Joris et al. 1994, e.g.). We idealize these anatomical and physiological observations to argue that MSO neurons are arranged with spatial symmetry and their inputs arrive in synchrony with one another across a local subpopulation. These conditions of synchrony and symmetry justify the use of a simplified one-dimensional volume conductor model (Rall and Shepherd 1968).

The current balance relations for the intra- and extracellular domains of the MSO model (in terms of current density) are:

$$C_m \frac{\partial V_m}{\partial \tau} = G_{Lk}(V_m - E_{Lk}) + G_{KLT} w^4 z (V_m - E_K) + G_K (V_m - E_K) + \frac{d}{4R_i} \frac{\partial^2 V_i}{\partial x^2} + J_{in} \quad (14)$$

$$C_m \frac{\partial V_m}{\partial \tau} = G_{Lk}(V_m - E_{Lk}) + G_{KLT} w^4 z (V_m - E_K) + G_K (V_m - E_K) + \frac{d}{\kappa 4R_i} \frac{\partial^2 V_c}{\partial x^2} + J_i \quad (15)$$

with the same boundary conditions as the passive model (Eqs. 6 and 7). These equations and the dynamics of the gating variables w and z are adapted from a biophysically-based model of an MSO neuron first presented by Mathews et al. (2010) (see Eqs. 16-19 below). We have used the coupling coefficient κ in Eq. 15 as we did in Eq. 5 of the passive cable model to avoid the introduction of unknown parameters for extracellular resistance and population size. We will discuss plausible values for κ (see Fig. 1).

The neuron model consists of two dendrites extending away from a central soma. Each dendrite is a 150 μm -long cylinder with diameter $d = 3.5 \mu\text{m}$. The soma is a cylinder of length 20 μm and diameter $d = 20 \mu\text{m}$. Membrane capacitance is $C_m = 0.9 \mu\text{F}/\text{cm}^2$, intracellular (axial) resistivity is $R_i = 200 \Omega\text{cm}$, and leak conductance density is $G_{Lk} = 0.3 \text{ mS}/\text{cm}^2$. The neuron model includes low threshold K (KLT) current and hyperpolarization-activated cation (h) current. Maximal KLT conductance density is 17 mS/cm^2 in the soma and 3.58 mS/cm^2 in the dendrites, and maximal h conductance density is 0.86 mS/cm^2 in the soma and 0.18 mS/cm^2 in the dendrites. These parameters correspond to the “step-gradient” model in Mathews et al. (2010).

The KLT current has a voltage-gated activation variable w and inactivation variable z that evolve according to $du/dt = [u_\infty(V_m) - u]/\tau_u(V_m)$ where $u = w$ or z and

$$w_\infty(V_m) = [1 + e^{-(V_m + 57.34)/11.7}]^{-1} \quad (16)$$

$$\tau_w(V_m) = 21.5 [6e^{(V_m + 60)/7} + 24e^{-(V_m + 60)/50.6}]^{-1} + 0.35 \quad (17)$$

$$z_\infty(V_m) = 0.73 [1 + e^{(V_m + 67)/6.16}]^{-1} + 0.27 \quad (18)$$

$$\tau_z(V_m) = 170 [5e^{(V_m + 60)/10} + e^{-(V_m + 70)/8}]^{-1} + 10.7. \quad (19)$$

The gating variable for the h -current evolves slowly (time scale on the order of hundreds of milliseconds, see Khurana et al. 2011). We make the simplification, therefore, that G_h remains at a constant value in all simulations.

In most simulations the input current J_{in} is a simulated synaptic input with alpha function conductance:

$$I_{in} = G_{syn} \left(\frac{t - t_0}{\tau_{syn}} \right) \exp \left(1 - \frac{t - t_0}{\tau_{syn}} \right) (V_{rev} - E_{syn}). \quad (20)$$

G_{syn} is the maximal synaptic conductance density [mS/cm²], t_0 is the onset time of the synaptic event, τ_{syn} is the synaptic time constant, and E_{syn} is the reversal potential. Excitatory inputs to the MSO neurons are fast (Golding and Oertel 2012) and primarily target dendrites (Couchman et al. 2012). We set the synaptic time constant in Eq. 20 to $\tau_{syn} = 0.2$ ms, consistent with *in vitro* physiology and previous modeling studies (Jercoc et al. 2010; Fischl et al. 2012; Myoga et al. 2014) and the reversal potential is 0 mV. In some simulations the onset times t_0 of synaptic events are fixed (with a specific timing difference between inputs on the two dendrites, for instance) and in other simulations the onset times are drawn from Poisson processes to approximate more realistic input patterns. Exceptions are the simulations of spike time synchrony and time-difference tuning curves (Fig. 11) in which the alpha function conductance in Eq. 20 is replaced with a rectified sine wave that is meant to approximate the population-averaged conductance input to MSO in response to pure tone stimuli. We place excitatory inputs on either dendrite ~ 125 μ m from the soma. MSO neurons also receive inhibitory inputs (Grothe and Sanes 1993, 1994) that primarily target the soma (Couchman et al. 2012). We omit these in the current study. We have explored the contribution of inhibition to simulated V_e responses in an MSO model in previous work (Goldwyn et al. 2014).

To highlight ephaptic coupling in the MSO model we embed an additional “test” neuron in V_e . This single neuron’s contribution to V_e is $O(1/N)$ so can be neglected. We keep the properties of this test neuron the same as those in the population, but in some simulations we attach an additional compartment to the soma that contains spike-generating Na current. We use this test neuron to evaluate how ephaptic interactions alter coincidence detection in the MSO neuron model.

The additional compartment represents the putative spike initiation zone (SIZ). This likely corresponds to the axon initial segment and/or a proximal node of Ranvier (see Lehnert et al. (2014) for a recent computational study of spike initiation in an MSO neuron model). The membrane dynamics in the SIZ are

$$C_m \frac{\partial V_m^{SIZ}}{\partial t} = G_{IR} (V_m^{SIZ} - E_{IR}) + G_{Na} m^3 h (V_m - E_{Na}) - \frac{g_{axial}}{S_{SIZ}} (V_m^{SIZ} - V_i^{soma}). \quad (21)$$

V_i^{SIZ} is the membrane potential in the SIZ, V_m^{SIZ} is the SIZ membrane potential, and V_i^{soma} is the intracellular potential at the soma. The SIZ is influenced by the local extracellular voltage because $V_m^{SIZ} = V_i^{SIZ} - V_e$, where V_e is the extracellular voltage at the location of the SIZ.

The dynamics of the Na current (m and h variables) are modified from the Rothman and Manis model (2003). They are adjusted for a temperature of 35°C (Khurana et al. 2011) and the gating properties of the Na inactivation variable h are “left-shifted” by 6 mV. This modification is motivated by *in vitro* measurements (Scott et al. 2010) and enhances the phasic character of the model neuron (Huguet et al. 2012).

$$m_{\infty}(V_m) = [1 + e^{-(V_m+38)/7}]^{-1} \quad (22)$$

$$\tau_{in}(V_m) = 0.24 \left[\frac{10}{5e^{(V_m+60)/18} + 36e^{-(V_m+60)/25}} + 0.04 \right] \quad (23)$$

$$h_{\infty}(V_m) = [1 + e^{(V_m+71)/6}]^{-1} \quad (24)$$

$$\tau_k(V_m) = 0.24 \left[\frac{100}{7e^{(V_m-66)/11} + 10e^{-(V_m+66)/25}} + 0.6 \right] \quad (25)$$

The SIZ is assumed to be a small patch of membrane (1 μm diameter and 1 μm length, surface area is $S_{siz} = 3.14 \mu\text{m}^2$) with a dense concentration of Na channels. The leak conductance density is $G_{lk} = 200 \text{ mS/cm}^2$, the maximum Na conductance density is $G_{Na} = 75,000 \text{ mS/cm}^2$. The capacitance per area is $C_m = 0.9 \mu\text{F/cm}^2$. These parameters are chosen so that the characteristics of the backpropagating action potential in the soma are similar to *in vitro* recordings (Scott et al. 2007). The current balance equation for the soma of the test neuron is also altered to account for axial current flow to and from the SIZ with $g_{axial} = 60 \text{ nS}$. Reasonable assumptions are that the initial segment's diameter is $\sim 1\text{-}1.5 \mu\text{m}$ (Lehnert et al. 2014) and the axial resistance connecting the SIZ to the soma is $200 \Omega\text{cm}$. For these values and $g_{axial} = 60 \text{ nS}$, the implied length of the soma-to-SIZ connection is $\sim 6\text{-}15 \mu\text{m}$, consistent with the anatomy of the initial segment reported by Lehnert et al. In our simulations we take a phenomenological view of the SIZ and allow its location in the V_e field to be more distant from the soma. The intracellular connection between the SIZ and the soma (i.e. g_{axial}) remains the same in all simulations regardless of the location of the SIZ in the extracellular domain.

We assume that spikes do not contribute significantly to V_e . We do not, therefore, include spikes in the MSO population and do not take into account spikes generated in the SIZ of the test neuron when computing V_e . This assumption is based on a consensus that post-synaptic membrane currents in the MSO generate the prominent, ongoing sound-evoked V_e in the auditory brain and spikes do not significantly contribute to it (Galambos et al. 1959, Mc Laughlin et al. 2010, e.g.). Physiological observations support the assumption that spikes do not contribute to V_e . Back-propagating action potentials in the soma of MSO neuron are small ($\sim 20 \text{ mV}$) when measured *in vitro* (Scott et al. 2007) and *in vivo* (Franken et al. 2015) and can be difficult to detect in extracellular recordings (Yin and Chan 1990) and juxtacellular recordings (van der Heijden et al 2013).

Solution Method: As mentioned above, Eqs. 14 and 15 represent a system of PDAEs. Due to the voltage-gated ion currents and the synaptic (conductance) input, the coupling between intra- and extracellular voltages is nonlinear and V_m -dependent. To solve these equations, we discretize the spatial domain in small bins

of length Δx . This converts the PDAEs into a system of differential algebraic equations (DAEs) that can be solved with appropriate software (we use SUNDIALS, available at <http://computation.llnl.gov/casc/sundials/main.html>, Hindmarsh et al. 2005). The discretization is analogous to the compartmental method for computing V_m dynamics in a spatially-extended neuron model (Segev and Burke 1998), but in our formulation intracellular and extracellular compartments reside at each point in discretized space and are coupled to one another. The numerical method is designed to conserve the flow of current in and out of each compartment, so it is necessary to define intra-, extra-, and membrane currents (I_i, I_e, I_m) [units of milliamperes].

Let x identify the spatial location of a compartment of width Δx . Then we denote the intracellular (axial) current flow from an adjacent compartment into the compartment at x as:

$$I_i(x - \Delta x/2, t) = \frac{V_i(x - \Delta x, t) - V_i(x, t)}{r_i \Delta x} \quad (26)$$

and extracellular current flow as:

$$I_e(x - \Delta x/2, t) = \frac{V_e(x - \Delta x, t) - V_e(x, t)}{\kappa r_i \Delta x}. \quad (27)$$

For notational simplicity we have substituted r_i for $4R_i/\pi d^2$ in these and subsequent equations. Note that, unlike the cable equation, the diameter d of each compartment is not uniform (soma is larger than dendrites). As a result, r_i and the coupling parameter κ are larger in the soma compartments than in the dendrite compartments. For ease of notation we do not explicitly indicate this x -dependence of r_i and κ .

The net flows of intra- and extracellular currents at location x satisfy current balance relations with the transmembrane current $I_m(x, t)$:

$$I_{in}(x, t) = \frac{V_i(x - \Delta x, t) - 2V_i(x, t) + V_i(x + \Delta x, t)}{r_i \Delta x} \quad (28)$$

$$I_m(x, t) = \frac{V_e(x - \Delta x, t) - 2V_e(x, t) + V_e(x + \Delta x, t)}{\kappa r_i \Delta x}. \quad (29)$$

The transmembrane current $I_m(x, t)$ at location x (by convention, outward flow of positive ions is positive current) consists of capacitative, leak, ionic, and input currents:

$$I_m(x, t) = S \left[C_m \frac{dV_m}{dt} - g_{leak} (V_m - E_{leak}) + g_{Na} \sigma^2 (V_m - E_{Na}) + g_{K} \sigma (V_m - E_{K}) \right] + I_{in} \quad (30)$$

S denotes surface area of the MSO compartment and it depends on x ; it is larger in soma compartments than in dendrite compartments. I_{in} is the input current in units of milliamperes.

By identifying the right side of Eq. 30 with the second-order differences in Eqs. 28 and 29, we obtain a set of equations that dynamically couple intracellular and extracellular voltage via the membrane potential. We impose boundary conditions as in the cable model: a ‘‘sealed end’’ for V_i in the intracellular domain

and a linear decay of V_e to ground (0 mV) at a distance of 1 mm from the ends of the dendrites. To include the test neuron with SIZ, we solve two versions of the intracellular model, one for the population MSO response (the generators of V_e) and one for the test neuron. The test neuron includes coupling to its SIZ given by Eq. 21. The SUNDIALS numerical solver steps forward in time while maintaining these current balance relations by using a variable order, variable coefficient implicit method (Hindmarsh et al. 2005). We used a relative tolerance of 10^{-6} and an absolute error tolerance of 10^{-8} in the solver and obtained the solution at $1\mu\text{s}$ time steps.

MATLAB code is available on the ModelDB repository and includes example solutions of the MSO model and user-friendly simulation code for the passive cable model.

RESULTS

Ephaptic interactions in passive cables

Remarks on coupling parameter κ : The coupling parameter $\kappa = Nr_e/r_i$ dictates the strength of interactions between V_e and V_m . The standard cable theory assumes that V_e is spatially uniform and negligible. This is the limiting case of $\kappa \rightarrow 0$. To estimate a range of plausible non-zero values of κ , we introduce two new parameters: the packing density δ of the population of N cables and the ratio of extracellular to intracellular volume resistivities $\rho = R_e/R_i$. Let A_i be the cross-sectional area of each cable and A_e the cross-sectional area of the extracellular space (i.e. the total cross-sectional area of the brain region under consideration is NA_i+A_e). Then, the relations $r_u = R_u/A_u$ ($u = i, e$) and $\delta = NA_i/(NA_i+A_e)$ allow us to express the coupling parameter as $\kappa = \rho\delta/(1-\delta)$. The advantage of this formulation is that we can estimate bounds on ρ and δ .

Extracellular resistivity R_e has been measured in a number of biological tissues and animals (Geddes and Baker 1967, e.g.). Based on these and other experiments, modeling studies typically use values of ρ that range from ~ 1 to 4. In simulations of neuron- V_e interactions, Holt and Koch (1999) used $\rho = 2.2$ ($R_i = 150 \Omega\text{cm}$ and $R_e = 330 \Omega\text{cm}$). Recent modeling studies of cortical local field potentials have used similar values: $\rho = 2.2$ in Lindén et al. (2010) and $\rho = 3.5$ in Reimann et al. (2013), for example.

The packing density δ of a local population of neurons depends on their spatial arrangement and morphology. For the idealized case of uniform cables oriented in parallel to one another we can provide a theoretical upper bound by treating the population of cables as an example of circle packing in a plane (when viewed in cross-section). In this case, the theoretical upper bound for δ is ~ 0.9 (Weisstein). If the extracellular domain is a circle then the upper bound for δ would be closer to 0.8 for a moderate (<100) number of cables (Graham et al., 1998). Figure 1 shows a contour plot of κ as a function of ρ and δ in these parameter ranges. For small packing densities and small ρ the coupling strength approaches 0, but κ exceeds 1 in over half of the parameter space and can reach values as large as ~ 15 . Unless otherwise specified, we will gauge ephaptic effects in the cable model

by comparing simulations without V_e coupling ($\kappa = 0$) to simulations with $\kappa = 1$. Our estimates for κ in the MSO model are also within this plausible range. They are marked in Fig. 1 and discussed below.

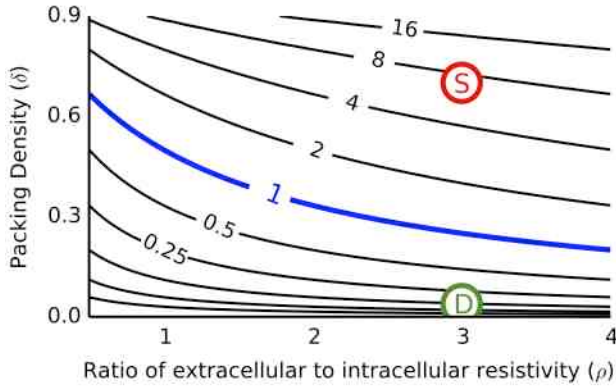


Figure 1: Contour plot of the coupling parameter κ for plausible values of packing density (δ) and resistance ratio (ρ). Coupling parameter is $\kappa = \rho\delta/(1-\delta)$, contour lines have logarithmic spacing (powers of 2). We use $\kappa = 1$ (blue contour) in simulations of the cable model with ephaptic coupling. Estimates for κ in the MSO model are marked with colored circles. κ is larger surrounding the soma (7, red S) than the dendrite (0.12, green D) since the larger diameter of the soma implies a larger packing density ($\delta = 0.7$ for soma and 0.038 for dendrites; $\rho = 3$ throughout).

Responses to constant current – Initial observations: We begin our investigation of ephaptic interactions by studying responses to constant current applied at a single point along the cable. Responses in this scenario are solutions to the boundary value problem for the coupled intra- and extracellular voltages at steady state given in Eqs. 8-10. The space constant in MSO neurons is roughly the length of one dendrite (Mathews et al. 2010). We use the cable to gain initial insights that can be applied to the MSO, so we set the space constant λ in the cable model to be one-half the physical length of the cable, unless otherwise indicated. Steady state solutions do not depend on the cable time constant τ .

We first injected a constant, depolarizing current to a site near the left end of the cables in the population (schematic in Fig. 2A). The population-averaged V_m is maximal at the site of the input and attenuates with distance along the cable (Fig. 2B). The stimulus amplitude in these simulations is arbitrary; response amplitude scales linearly with stimulus amplitude for current injection to passive cables.

The effect of coupling all cables in the population via V_e is evident in the difference between the population-averaged V_m response in the absence of coupling ($\kappa = 0$, black line in Fig. 2B) and the response with ephaptic coupling ($\kappa = 1$, blue line in Fig. 2B). Ephaptic coupling increases the membrane depolarization V_m near the stimulation site, acting to increase the input resistance. At locations distant from the input site, ephaptic coupling decreases the depolarization of V_m . The net result of ephaptic coupling is to increase the rate at which V_m attenuates with distance along the cable. In other words, ephaptic coupling decreases the cable space constant, effectively increasing the electrotonic length of the cable. This effect of V_m -to- V_e coupling was noted by Rall in his example of an “axon in oil” (Rall 1977). In that analysis of an infinite cable surrounded by a thin extracellular layer, Rall noted that the space constant of the cable decreases as extracellular resistance increases

according to $\sqrt{r_m/(r_1 + r_2)}$, or equivalently $\sqrt{(R_m/\pi d)/(R_i/\Lambda_i + R_o/\Lambda_o)}$ where d is the cable diameter.

We highlight the ephaptic effect by showing the response of a “test neuron” embedded in the V_e field generated by all neurons in the population. The test neuron’s membrane potential V_m (more precisely, the deviation of V_m from rest) displays the same changes discussed above: a local depolarization near the site of input current and hyperpolarization at more distant locations on the cable (Fig. 2C). This cable has identical properties to the cables whose population-averaged V_m is shown in Fig. 2B. The test neuron does not receive any current injection. The V_e surrounding the test neuron is the sole “input” that determines the spatial profile of V_m in Fig. 2C. We point out that ephaptic coupling hyperpolarizes V_m at the center of the cable ($V_m < 0$ mV at $x/\lambda = 1$). This anticipates a main finding in our MSO simulations: V_e produced by dendritic excitation can have a hyperpolarizing or “inhibitory” effect on the soma of a “nearby” MSO neuron.

We can understand the ephaptic effects in these simulations by examining the spatial profile of V_e in Fig. 2D. The input current is a transfer of positive ions from the extracellular domain into the interior of the population-averaged cable and thus V_e is negative near input site; the input acts as a current sink to the surrounding extracellular domain. Recall from Eq. 2 the heuristic that the second spatial derivative of V_e acts as a distributed “ephaptic current” to perturb membrane potential (neglecting boundary effects). The second spatial derivative of V_e at this minimum is positive and thus the test neuron “feels” V_e as a depolarizing current at the input location. Conservation of current in the system requires that the flow of current from the extracellular domain into the cables (i.e. the stimulus current) must be returned back to the extracellular domain at other locations along the cable. As a result, V_e is positive at spatial locations distant from the stimulus site. At these distant locations the extracellular space draws current out of the test neuron and hyperpolarizes V_m ; the efflux acts as a current source to the extracellular surround.

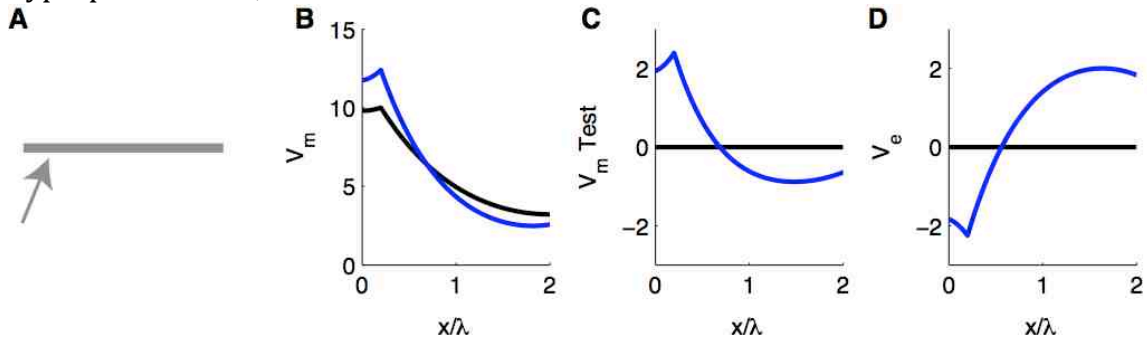


Figure 2: Passive cable response to constant input current. Responses without ephaptic coupling ($\kappa = 0$) shown in black, responses with ephaptic coupling ($\kappa = 1$) shown in blue. **(A)** Input location is near one end of cable. **(B)** Steady-state depolarization of population-averaged V_m . **(C)** Steady-state V_m response of “test neuron” that is coupled to population of cables via the extracellular voltage. V_m in B and C are plotted as deviations from resting potential. **(D)** Steady-state V_e response produced by population of cables. Abscissa in all panels is distance along the cable normalized by the cable space constant λ (one-half the physical length of the cable).

In these simulations, a relatively modest input current and coupling parameter (~ 12 mV maximum depolarization in population-averaged response, $\kappa =$

1) produces V_e amplitudes of ± 2 mV. The amplitude of the response of the test neuron is similar to V_e : ~ 2.5 mV maximum depolarization and ~ -1 mV hyperpolarization. This result is consistent with the observation made by Anastassiou et al. (2010) that the spatial frequency of V_e must be sufficiently large, relative to the electric and physical lengths of the cable, to perturb V_m . More precisely, they showed that a spatially inhomogeneous V_e with spatial frequency f_s has an $O(1)$ effect on V_m of a passive cable if the dimensionless angular spatial frequency of V_e ($\Omega = 2\pi f_s \lambda$) is larger than 1 and $1/L$, where L is the cable's physical length normalized by its space constant λ . Both conditions are satisfied in these simulations because L in our cable model is twice the cable space constant. This implies $1/L$ is one-half (less than one). In addition, the spatial profile of V_e in Fig. 2D (although not exactly a sine wave) appears somewhat like a half-cycle of a periodic waveform. We can say, therefore, that $f_s \lambda \approx 1$ and thus $\Omega > 1$.

If we move the stimulation site to different locations along the cable, the spatial angular frequency of V_e appears to always be about one-half to one times the length of the cable (Fig. 3D). Thus the effect of V_e on V_m remains roughly $O(1)$ in all cases, as shown in the responses of the test neuron in Fig. 3C. This generic feature of the V_e spatial profile generated by the cable population is due to conservation of current and the geometry of the one-dimensional volume conductor. Depolarizing input current reduces V_e near the input site and the return of current back to the extracellular space restores V_e to zero or positive values at locations of the cable distant from the input site. These V_e effects can also be seen in the population-averaged V_m responses by comparing responses that include ephaptic coupling (thick lines in Fig. 3B) to those that do not include ephaptic coupling (thin lines).

For the different input locations in Fig. 3, the spatial pattern of V_e changes dramatically in the extracellular region beyond the ends of the cable (not shown). In these simulations, the distance from the ends of the cable to electric ground is two times the space constant (i.e. same as physical length of cable). For off-center inputs (blue and green), V_e is non-zero beyond the ends of the cable as it decays linearly to 0 mV at electric ground. For inputs to the center of the cable (red), V_e is 0 mV at the ends of the cable and remains zero at all spatial locations beyond the ends of the cable. This is reminiscent of a "closed field" configuration. The responses to off-center inputs have V_e spatial profiles that extend broadly beyond the ends of the cables and would be classified as an "open field" configuration (Lorente de Nò 1947). We note that for this linear problem (passive cable with current input), a more complicated spatial pattern of inputs can be constructed by taking the appropriate sum of responses to "point current" inputs.

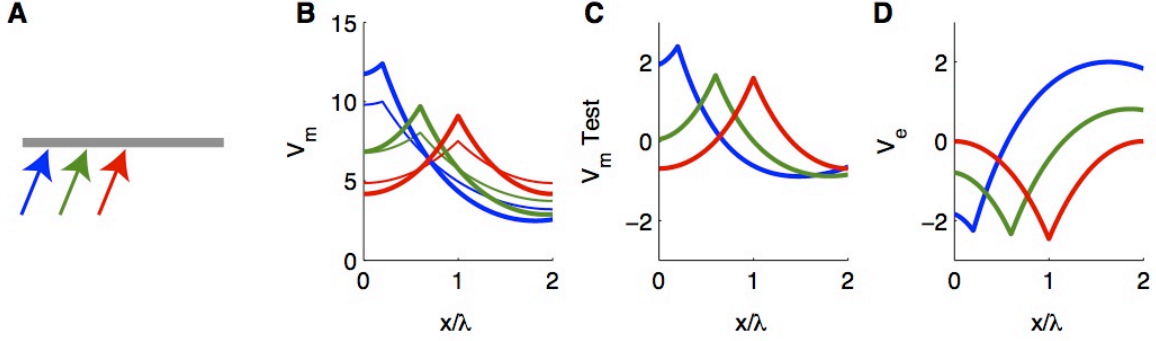


Figure 3: Passive cable response to constant input current for varying input location. **(A)** Input location is near end of cable (blue, same as Fig. 2), intermediate (green), or at center of cable (red). **(B)** Steady-state depolarization of population-averaged V_m . Thick lines are responses with ephaptic coupling ($\kappa = 1$) and thin lines are responses without ephaptic coupling ($\kappa = 0$). **(C)** Steady-state V_m^{Test} responses of “test neuron” that is coupled to population of cables via the extracellular voltage. **(D)** Steady-state V_e responses produced by population of cables. Beyond the ends of the cable (not shown), V_e decays linearly to electric ground (0 mV) for off-center inputs and remains at 0 mV for centered input.

Ephaptic interactions are greatest for electrotonically compact cables: It is known that the cable properties of a neuron model influence the amount to which its membrane potential is perturbed by a fixed, applied V_e . In particular, previous studies of passive cables embedded in V_e found that the effect of V_e on V_m increases with the cable space constant (sinusoidal V_e in Anastassiou et al. 2010; linear V_e in Frölich and McCormick 2010). We show in Fig. 4 that the same result holds for endogenous V_e generated in response to constant current input.

We keep the space constant of the cable population identical in all simulations (twice the physical length of the cables in the population), and obtain population-averaged V_m and V_e responses to constant, depolarizing current injection (Fig. 4A and Fig. 4C). This value of the space constant is our “reference” space constant λ_{ref} . The x -axis in all panels of Fig. 4 shows distance along the cables normalized by λ_{ref} .

Keeping the properties of the cable population unchanged, we vary the space constant λ of the test neuron and observe changes in the test neuron’s response to endogenous V_e . Specifically, we show that compact cables are more susceptible to ephaptic interactions (Fig. 4B). The value for the space constant used in previous simulations is half the physical length of the cable (denoted as λ_{ref}). If the space constant of the test neuron is reduced to half this value, i.e. an electrically longer cable, the ephaptic effect on V_m^{Test} decreases (green line). If the space constant is twice as large as the reference value, i.e. an electrically shorter cable (red line), the ephaptic effect on V_m^{Test} increases.

These changes of V_m^{Test} with space constant reflect that the test neuron’s response to V_e is a balance between local membrane currents that drive the membrane potential back to rest (0 mV in these figures since V_m^{Test} is plotted as deviation from rest) and axial intracellular currents that drive V_m^{Test} toward a constant spatial profile. In the limit of an electrotonically compact test neuron (large space constant), V_m^{Test} approaches a uniform spatial profile because intracellular current is easily redistributed along the cable. More precisely, for large λ the deviation of V_m^{Test}

from E_{lk} for the test neuron approaches $-V_e + \frac{1}{L} \int_0^L V_e dx$. This value, which represents the upper bound on how much V_e can perturb \bar{V}_m of the test neuron is shown as a thin black line in Fig. 4B.

In the opposite limit of an electrotonically long test neuron (small space constant), the local membrane currents dominate (relative to axial current flow). \bar{V}_m remains near its resting potential over most of the cable, but is perturbed near the input site and cable terminals. These observations regarding the sensitivity of the test neuron to V_e also match our intuition from thinking of V_e as a distributed “ephaptic current.” Recall Eq. 2: an increase of r_i (by reducing axial conductance, for instance) decreases the amplitude of the term $\frac{1}{\tau_i} \frac{\partial^2 V_e}{\partial x^2}$. Thus neurons with small space constants due to large internal resistance r_i are unresponsive to V_e .

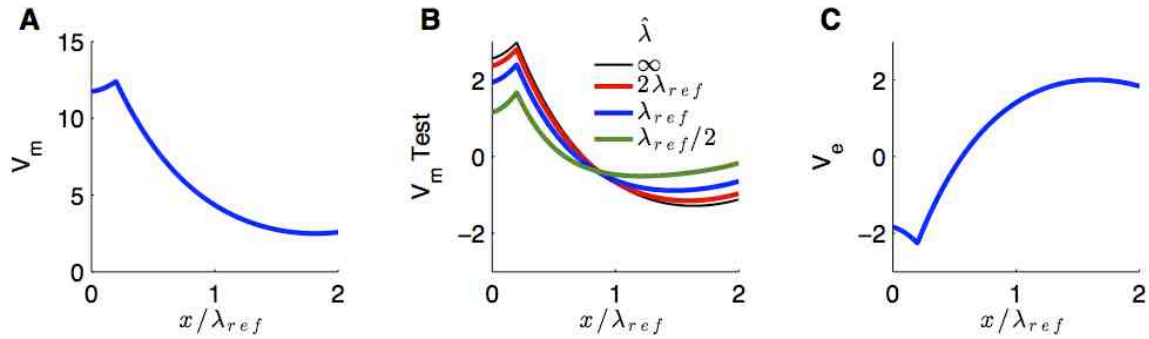


Figure 4: Passive cable response to constant input current for varying space constant $\hat{\lambda}$ of test neuron. **(A)** Steady-state depolarization of population-averaged V_m , same as Fig. 2B. **(B)** Steady-state response of “test neuron” \bar{V}_m . Space constant $\hat{\lambda}$ of test neuron is varied so that it is smaller (green), same (blue) or larger (red) than space constant of cables in population. Space constant for cables in population is λ_{ref} (half the physical length of the cable) in all simulations. **(C)** Steady-state V_e response produced by population of cables, same as Fig. 2D. Abscissa shows dimensionless distance along cable relative to the reference space constant (half the physical length of all cables).

A novel feature of our model is that V_e is not imposed as an exogenous input. V_e is generated endogenously by the activity of a population of cables. We can also explore, therefore, how the spatial profile of V_e depends on the space constant λ of the cable population that generates V_e . We find the amplitude of V_e increases with λ , as shown in Fig. 5C and Fig. 5F. Roughly speaking, we can imagine the cable population acts as a current dipole. A large space constant increases V_e amplitude because it increases the dipole moment by allowing current to flow more easily within the cable (axially). As an illustration of this analogy, we mark the location of the current sink (site of current injection) by a black minus sign in Fig. 5C and Fig. 5F. We then computed the center of mass of source currents, where we defined source currents by $\max(0, -\frac{1}{r_i} \frac{\partial^2 V_e}{\partial x^2})$. We marked these locations with colored plus signs. Consistent with analogy to the dipole moment, the location of the source moves away from the sink with increases in the cable space constant.

We vary λ in two ways: by altering the membrane resistance r_m (upper row of Fig. 5), or by altering the intracellular (axial) resistance r_i (lower row of Fig. 5). The population-averaged V_m responses change dramatically depending on which parameter is manipulated (compare the red curves in Fig. 5A and Fig. 5D, for

instance, and note that the input current is identical in all simulations). In the top row, increases of λ are associated with increases of r_m and, consequently, increases of the cable input resistance (Rall 1977). In the bottom row, increases of λ are associated with decreases of r_i and, consequently, decreases of the cable input resistance. Recall that the coupling strength is inversely proportional to r_i , so for Fig. 5D-F we changed κ to $1/4$ for the case of small λ and $\kappa = 4$ for the case of large λ .

Although population-averaged V_m responses change with these parameter manipulations, the V_e responses remain similar for equal values of λ . Regardless of whether r_m or r_i is varied, the steady state distribution of transmembrane currents (steady-state, in these simulations) remains similar for a fixed λ . Since V_e is generated by this current distribution, V_e does not depend strongly on r_m and r_i as long as λ remains at a fixed value.

In these simulations, the space constant of the test neuron is set to the reference value (half the physical length of the cable). Nonetheless, the perturbation of V_m from rest increases for larger values of the cable population space constant (Fig. 5B and Fig. 5E). If we were to allow the test neuron space constant to co-vary with the cable population, we would see a “double effect” of ephaptic coupling. As the space constant of the population and test neurons increased together, the test neuron would be more susceptible to the effects of V_e (recall Fig. 4B) and the amplitude of V_e would increase (Fig. 5C and Fig. 5F).

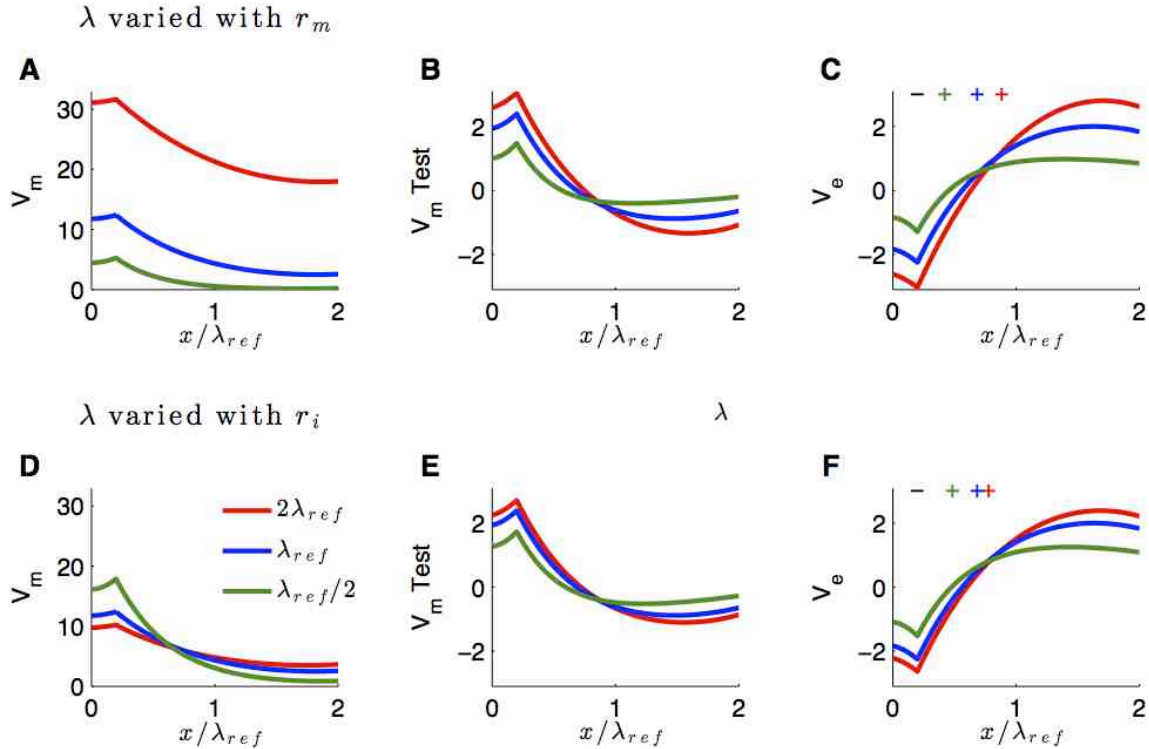


Figure 5: Passive cable response to constant input current for varying space constant of the cable population. The test neuron space constant is fixed at the reference value (half the physical length of the cable, denoted λ_{ref}) in all simulations. Space constants of the cable population are varied by changing r_m (top row) or r_i (bottom row). **(A, D)** Steady-state depolarization of population-averaged V_m . **(B, E)** Steady-state V_m response of test neuron. **(C, F)** Steady-state V_e response produced by population of cables. The minus signs mark the location of the current sink (current injection). The plus signs mark the center of mass of source currents (see text for explanation). Abscissa shows dimensionless distance along cable relative to the reference space constant.

Responses to sinusoidal current – Initial observations: We have gained helpful initial insights by studying steady-state responses to constant current injection, but ultimately we are interested in dynamic ephaptic interactions (e.g. responses to trains of synaptic events). As a next step, therefore, we investigate responses of the cable population to sinusoidal current injection (Fig. 6). V_m , \bar{V}_m , and V_e in this case are solutions to the boundary value problem Eq. 11-13. We visualize these solutions by plotting amplitude (Fig. 6A-C) and phase (Fig. 6D-F) as functions of normalized distance along the cable. Phase is in units of radians with zero-phase equal to the starting phase of the sinusoidal stimulus. We plot time courses of V_m , \bar{V}_m , and V_e selected from three locations along the cable in Fig. 6G-I.

Responses to time-varying stimuli depend on the time constant $\tau = c_m r_m$ of the cable. In these simulations we set $\omega\tau = 0.1$, where ω is the stimulus frequency. This is an example in which the stimulus frequency is slow relative to the cable time constant. MSO neurons have exceptionally fast membranes (submillisecond time constants). We expect, therefore, that these simulations can provide intuition for MSO responses to stimulus frequencies as high as several hundred Hertz.

In the absence of ephaptic effects, the population-averaged V_m attenuates along the length of the cable ($\kappa = 0$, black line in Fig. 6A). The speed at which V_m propagates along the cable is evident in the roughly linear decay of phase along the cable (Fig. 6D). If ephaptic coupling is included ($\kappa = 1$, blue lines), the test neuron membrane potential and the extracellular voltage are non-zero. We remarked previously that ephaptic coupling effectively decreases the space constant of the cable (Rall 1977). This can be seen in the steeper attenuation of V_m amplitude in for $\kappa = 1$. A smaller space constant is also associated with slower propagation of voltage along a cable (Koch 1998). Slowing of voltage spread due to ephaptic coupling is apparent in the steeper slope of the phase profile in Fig. 6E for the simulation with $\kappa = 1$ compared to the simulation with $\kappa = 0$.

The V_e amplitude profile has two peaks (Fig. 6C) that correspond to two (roughly) anti-phase oscillations (note the abrupt, half-cycle phase transition in Fig. 6F). These anti-phase oscillations can be seen in time courses of V_e by comparing responses near the input site to responses distant from the input site (Fig. 6I). This response profile is an indication that the cable population acts like a collection of synchronized current dipoles (Mc Laughlin et al 2010). The spatial location of the minimum of the V_e amplitude profile is similar to the location of the half-cycle phase transition. For very low frequencies it would align with the location of the zero-crossing of the steady-state V_e response in Fig. 2D.

The \bar{V}_m response of the test neuron (Fig. 6B, E, H) has similar characteristics as the V_e response. In particular, it is comprised primarily by two anti-phase oscillations (note the two peaks in the amplitude profile and the corresponding half-cycle phase transition). It can be helpful to distinguish these two “modes” by which ephaptic coupling drives \bar{V}_m in the test neuron. On the proximal side, the test neuron membrane potential oscillates nearly in phase with the population-average membrane potential (compare green time courses in Fig. 6G and H). In contrast, the central and more distant regions of the test neuron oscillate anti-phase relative to the left side of the test neuron (compare red and cyan lines to green in Fig. 6H). In

the transition region between these two oscillatory “modes,” there is a minimum in the V_m amplitude profile. For very low frequencies, this minimum would approach 0 mV at the location of the zero-crossing in the stationary response (Fig. 2C). In response to time-varying inputs, however, there is spread of voltage along the cable and V_m is not equal to 0 mV at one fixed location for all time.

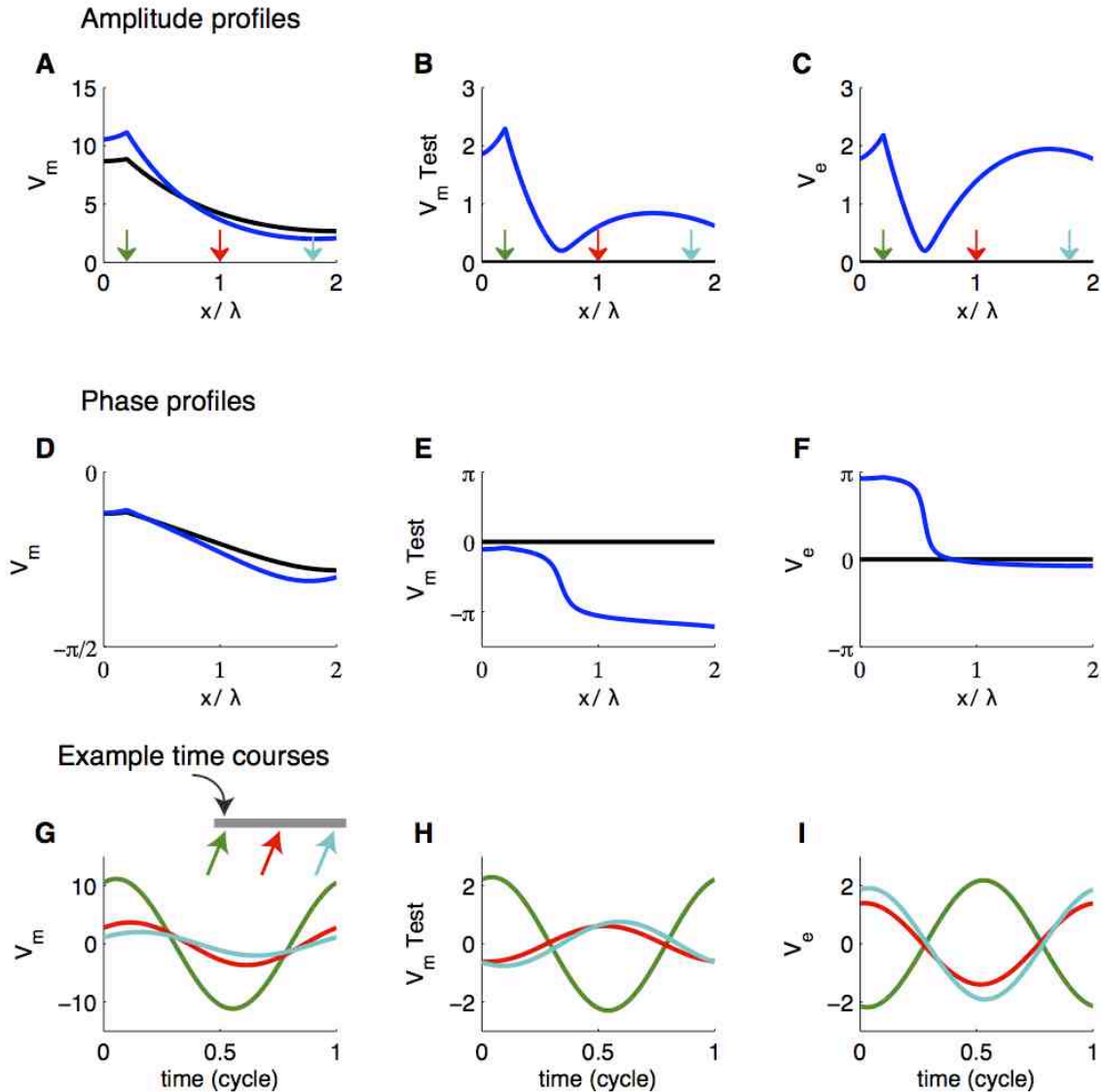


Figure 6: Passive cable response to sine-wave input current. Input frequency in dimensionless units is $\omega\tau = 0.1$. **(A-C)** Amplitude profiles of cable population (V_m), test neuron (V_{Test}), and extracellular voltage response (V_e). Membrane potentials are plotted as deviation from rest (units: mV). **(D-F)** Phase profiles cable population (V_m), test neuron (V_{Test}), and extracellular voltage responses (V_e). Phase is in units of radians and zero-phase is referenced to the stimulus phase. In Panels A-F, the x-axis is the dimensionless distance along the cable (distance normalized by the space constant). Black lines show responses without ephaptic coupling ($\kappa = 0$) and blue lines show responses with ephaptic coupling ($\kappa = 1$). **(G-I)** Time courses of V_m , V_{Test} , and V_e plotted at three locations along the cable. Abscissa is one cycle of oscillations, ordinate is in units of millivolt (deviation from rest for population-averaged and test neuron). Schematic in G shows input location (black arrow). Time course locations are marked by colored arrows in A-C and G. They are $X = 0.2, 1, \text{ and } 1.8$, where $X = x/\lambda$ is a dimensionless measure of distance along the cable.

Attenuation of high frequency responses due to low pass cable dynamics:

Responses to higher frequency stimuli are attenuated by capacitive filtering of the passive cable (Fig. 7). The amplitude of population-averaged V_m decreases with increasing frequency at all locations along the cable (Figs. 7A and 7D).

Extracellular voltage (Figs. 7C and 7F) and the test neuron V_{Test} (Figs. 7B and 7E) responses exhibit slightly more complex changes with stimulus frequency. We remarked previously that the V_e responses to low frequency inputs are dipole-like and that the ephaptic interaction in these cases evokes two anti-phase “modes” of oscillation in test neuron V_{Test} of the test neuron. As stimulus frequency increases, these dipole-like response features are distorted. In particular, when the time scale of the stimulus and the test neuron’s cable dynamics are similar (green curve, $\omega\tau = 1$), then the two “modes” of oscillation interact via spread of membrane potential along the cable. We have provided user-friendly simulation code to the ModelDB website so that the interested reader can view movies of these time-varying solutions.

We remark that at specific positions along the cable (say, the point aligned with the minimum of the black curve in Fig. 7C), V_e amplitude has a non-monotonic dependence on stimulus frequency. For the three locations we plot in Fig. 7F, however, V_e amplitude attenuates monotonically with stimulus frequency.

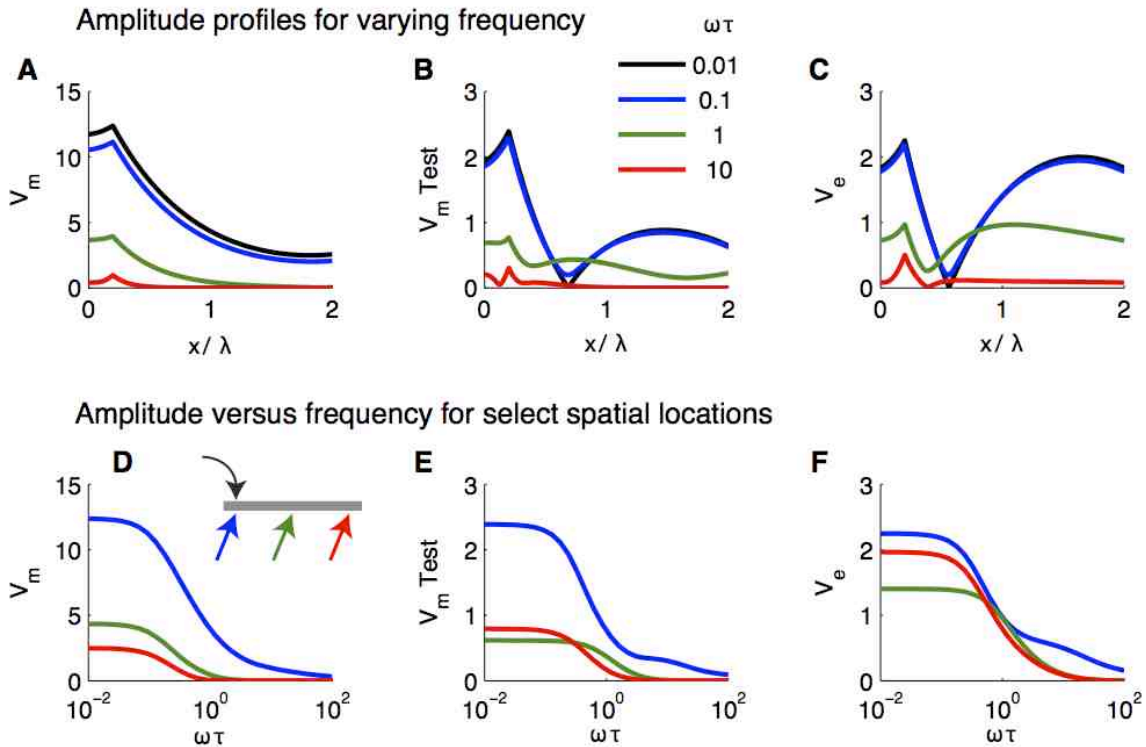


Figure 7: Attenuation of high frequency responses. **(A-C)** Amplitude profiles of cable population (V_m), test neuron (V_{Test}), and extracellular voltage responses (V_e). Membrane potentials are plotted as deviation from rest (units: mV). Different lines represent responses to different stimulus frequencies (see legend in B). **(D-F)** Amplitudes of V_m , V_{Test} , and V_e responses plotted against stimulus frequency for three locations along the cable. Input location (black arrows) and response locations (colored arrows) are indicated by the schematic in D, they are $X = 0.2, 1, \text{ and } 1.8$.

Ephaptic interactions in a model of medial superior olive

Initial simulations using a passive cable model have provided a basic understanding of the spatial and temporal patterning of ephaptic interactions in dendrite bundles. We next investigate ephaptic interactions in a biophysically-based model of the medial superior olive (MSO) to determine possible effects of V_e coupling in a specialized nucleus in the auditory brainstem.

Remarks on coupling parameter κ : Recall that the coupling parameter depends on the ratio of extracellular to intracellular resistivity (ρ) and the packing density of neurons δ according to the relationship $\kappa = \rho\delta/(1-\delta)$. Extracellular resistivity R_e in the auditory brainstem has not been measured, to our knowledge. As noted above, typical values of ρ in models of local field potentials in cortex are often in the range of 2.2 to 3.5 (Holt and Koch 1999; Lindén et al. 2011; Reimann et al. 2013). It is plausible that ρ in the MSO is larger due to the dense packing of myelinated fibers passing through the auditory brainstem, but we will use $\rho = 3$ as a reasonable estimate of the resistivity ratio.

We can estimate the packing density of neurons from an anatomical study of the MSO neurons in the gerbil (Rautenberg et al 2009). In that study, the mean soma diameter was 13 μm and the density of MSO neurons in a mature MSO slice was 7 cells per 100 μm . Consider, then, an idealized cross-section of MSO containing one column of 7 MSO somata (i.e. 100 μm length by 13 μm width). The packing density in this column is 0.715. In our simulations, we take $\delta = 0.7$ so that $\kappa = 7$ around the soma. Rautenberg et al. reported the diameter of dendrites in mature MSO slices was ~ 3 μm . The packing density of dendrites, and consequently the value of κ in regions surrounding dendrites, is smaller than the values estimated above for somata. If we again consider 7 cells distributed in a 100 μm by 13 μm column, then the packing density of dendrites is $\delta = 0.038$. We set $\rho = 3$ (the same value as we used for the soma) and estimate the coupling strength for dendrites to be $\kappa = 0.12$. These estimated values of κ near the soma and dendrites are marked in Fig. 1.

Responses to monolateral synaptic excitation: MSO neurons receive excitatory inputs that predominantly target their dendrites (Couchman et al. 2012). We begin our investigation of ephaptic coupling in MSO, therefore, by examining responses to a single excitatory synaptic event on one dendrite. The synaptic input depolarizes V_m in the dendrites of the population of MSO neurons (~ 30 mV near the input site). V_m amplitude attenuates as it spreads along the neuron (Fig. 8D, and evident in time courses at three locations along the neuron in Fig. 8A). V_m in the soma is ~ 9 mV and the finite propagation speed is evident as the peak of V_m is increasingly delayed as the post-synaptic potential propagates through the neuron.

The V_e response (Fig. 8C) is negative near the input site (blue curve) due to the local transfer of positive ions from the extracellular domain into the intracellular domain (current sink). Near the soma and opposite dendrite, V_e is positive (green and red curves) due to combined contributions of return currents distributed across the neuron (current sources). Recall that the coupling parameter in the dendrites is small ($\kappa = 0.12$). Nonetheless, the stimulation strength used in this simulation

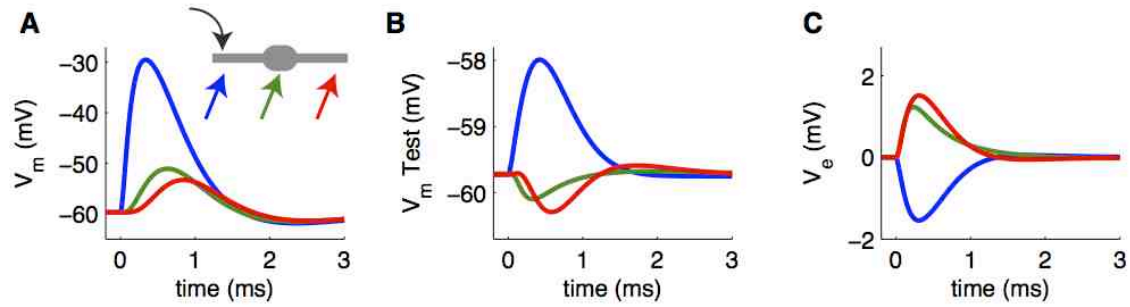
(maximal conductance is 27 mS/cm²) suffices to generate V_e amplitudes of ± 0.8 mV in the extracellular domain surrounding the dendrites.

The “test” MSO neuron receives no direct synaptic input; its membrane potential V_m (Fig. 8B) is perturbed by the spatio-temporal pattern of the surrounding extracellular voltage. V_m increases near the stimulation site and decreases in the soma and distal dendrite. The peak ephaptic “excitation” is ~ 1 mV. This illustrates that the millivolt-scale V_e responses observed *in vivo* in the MSO (Mc Laughlin et al. 2010, e.g.) could, in principle, represent a non-synaptic mechanism by which MSO neurons could induce millivolt-scale perturbations in membrane potential of neighboring neurons.

These simulations illustrate the dynamics of V_m , V_m , and V_e responses to simulated synaptic inputs. Many of the main qualitative features, however, were already present in the steady state passive cable simulations presented at the outset. To highlight the useful insights provided by the steady-state cable model, we plot spatial profiles of the maximum deviation from rest for the MSO neuron model in the bottom row of Fig. 8. These results can be compared to steady state passive cable responses (Fig. 2). Simulations without ephaptic coupling are shown in black and simulations with ephaptic coupling are shown in blue.

The deviation from resting voltage of the MSO neuron and passive cable models share many of the same qualitative features. For instance, in both cases the test neuron V_m amplitude in the soma (or center of passive cable) is negative. This indicates that ephaptic coupling (in this scenario of monolateral dendritic excitation) diminishes the response at the soma and may raise the threshold for MSO spiking. We will explore this in more detail below (see Figs. 10 and 11). There are, of course, quantitative differences. The profiles of V_m , for example, show that ephaptic effects are smaller in the MSO model than in the cable model (compare blue and black lines in Fig. 8D and Fig. 2B). The weaker ephaptic effect in the MSO model is likely due to the small coupling coefficient κ for MSO dendrites. Perhaps surprisingly, the V_m responses of the test neuron is largest in the dendrite (near the site of synaptic input) despite the small κ value there.

Example time courses



Maximum deviation from rest

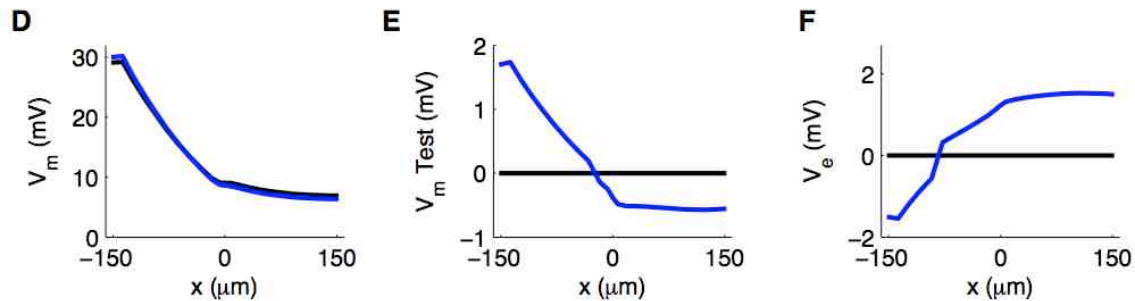


Figure 8: MSO response to monolateral synaptic excitation. **(A-C)** Example time courses of V_m in MSO population, V_m in the test neuron, and extracellular V_e at three locations along the neuron. Schematic in A shows these locations (left dendrite near the input site, soma, and right dendrite) and input location (left dendrite). Input to MSO population is a simulated excitatory synaptic event located $137.5 \mu\text{m}$ from the center of the soma with peak conductance 27 mS/cm^2 . Test neuron receives no synaptic stimulation. **(D-F)** Spatial profiles of maximum deviation from resting voltage for V_m , V_m , and V_e in response to monolateral synaptic excitation. Ordinate is deviation from resting voltage and can be compared to steady state passive cable responses in Fig. 2. Results for simulations without ephaptic coupling are in black, results for simulations that include ephaptic coupling are in blue.

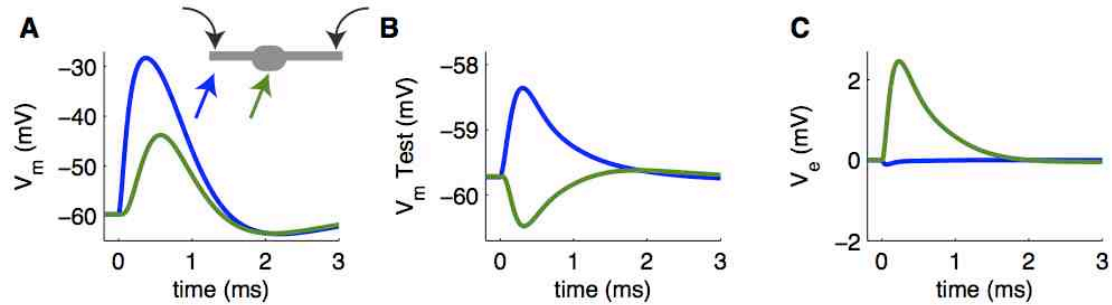
Responses to bilateral synaptic excitation: In natural listening conditions, MSO neurons receive excitation on both dendrites (from sounds arriving in both ears). In Fig. 9 we show responses to coincident bilateral inputs (simulated excitatory synaptic events that arrive simultaneously on both dendrites). Example voltage time courses are shown in the top row and the bottom row shows the maximal deviation from resting voltage.

The synaptic inputs depolarize the V_m by $\sim 30 \text{ mV}$ near the synaptic site and a summed depolarization of $\sim 15 \text{ mV}$ in the soma (Fig. 9A, D). Responses to bilateral inputs differ slightly from the linear superposition of monolateral responses due to the presence of voltage-gated low threshold K current in the dendrites and soma.

A striking difference in these simulations compared to responses to monolateral inputs shown in Fig. 8 above is that V_e is spatially localized (Fig. 9C, F). V_e reaches a maximum value $\sim 2.5 \text{ mV}$ near the soma, but near the distal reaches of the dendrites V_e decreases to 0 mV . The symmetric arrangement of membrane currents produces a “closed-field” with no volume conduction beyond the dendrites’ terminal ends. Given the small V_e and small coupling parameter surrounding the dendrite, ephaptic effects on the dendrites might not be expected. This is not the case. The depolarization of V_m in the dendrites of the test neuron is, in fact, roughly

twice as large (in amplitude) as the hyperpolarization in the test neuron soma (compare blue curve to green curve in Fig. 9B).

Example time courses



Maximum deviation from rest

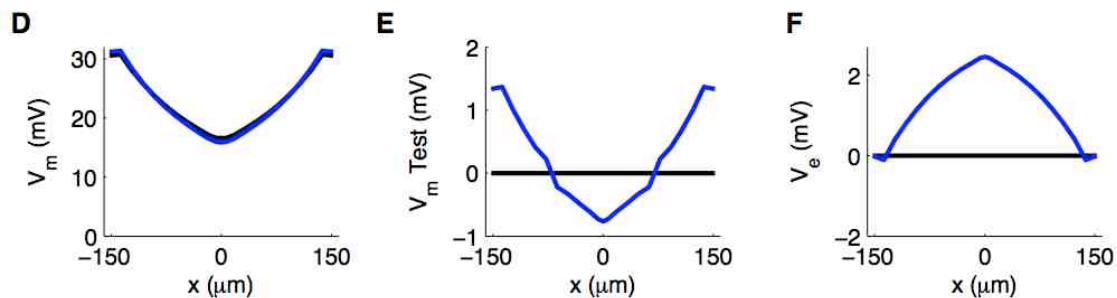


Figure 9: MSO response to bilateral synaptic excitation. **(A-C)** Example time courses of V_m in the MSO population, V_m^{Test} in the test neuron, and extracellular V_e at two locations along the neuron. Schematic in A shows these locations (left dendrite near the input site, soma) and input locations (both dendrites). Responses on right dendrite are identical to those on the left dendrite and are not shown. Inputs to the MSO population are two simulated excitatory synaptic events located $137.5 \mu\text{m}$ from the center of the soma on both dendrites. Synaptic events have identical maximal conductance (27 mS/cm^2) and onset time (0 ms). **(D-F)** Spatial profiles of maximum deviation from resting voltage for V_m , V_m^{Test} , and V_e in response to bilateral synaptic excitation. Results for simulations without ephaptic coupling are in black, results for simulations that include ephaptic coupling are in blue.

Ephaptic coupling influences MSO spike initiation: We have shown that endogenously-generated V_e can perturb the membrane potential of a “test” MSO neuron embedded in the extracellular bath. Does this ephaptic interaction suffice to alter spiking outputs of MSO neurons? By adding a spike-initiation zone (SIZ) to the test neuron model (see Methods), we can investigate how SIZ membrane potential and spiking activity is influenced by ephaptic interactions.

We created a situation in which V_e is generated from MSO neuron models that do not include an SIZ. We then embedded a test neuron with a SIZ into this V_e field (see Methods). The test neuron (including its SIZ) feels the influence of V_e but does not feedback and contribute to it. We are treating this one neuron’s contribution to V_e as sufficiently small that it can be ignored.

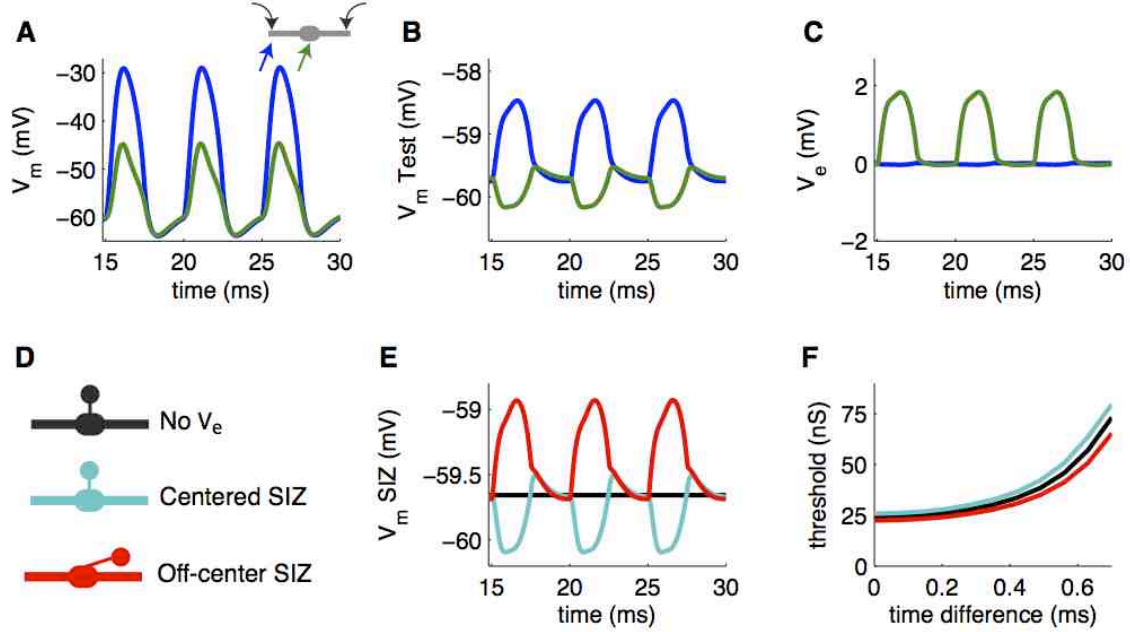


Figure 10: Response of MSO to periodic bilateral excitation. Test neuron includes a spike initiation zone (SIZ). **(A-C)** Time courses of V_m in the MSO population, V_m in the test neuron, and extracellular V_e at two locations along neuron. Schematic in A shows these locations: left dendrite near the input site (blue) and soma (green). Responses on right dendrite are identical to those on the left dendrite and are not shown. Waveform of excitatory conductance to MSO population is 200 Hz rectified sine wave (identical on both dendrites, located 137.5 μm from the center of the soma). Maximal conductance is 20 mS/cm^2 . Response is shown after 15 ms to avoid onset effects. **(D)** Schematic diagram illustrating the different SIZ and V_e configurations tested: no ephaptic coupling (black), ephaptic coupling and SIZ located in alignment with the soma at $x = 0 \mu\text{m}$ (cyan), ephaptic coupling and SIZ located $\sim 100 \mu\text{m}$ away from soma (red). **(E)** Membrane potential response in SIZ for three different model configurations. V_e coupling increases V_m in the SIZ for off-center SIZ and decreases V_m for centered SIZ. **(F)** Conductance threshold of test neuron in response to bilateral excitation. Inputs to test neuron are a pair of synaptic events (alpha function with 0.2 ms time constant, see Eq. 20) with time difference varied (x-axis).

We stimulate the MSO population with identical, synchronized excitatory conductance on both dendrites. The V_m response is a large ~ 30 mV depolarization in the dendrites that attenuates to a ~ 15 mV depolarization in the soma (Fig. 10A). The input conductance is a 200 Hz rectified sine wave identical on both dendrites (peak amplitude is 20 mS / cm^2). We use the rectified sine waveform as a simplified, population-averaged representation of excitatory drive to MSO in response to a pure tone stimulus.

The MSO population generates a periodic V_e response with ~ 1.8 mV positive going oscillations around the soma and much smaller negative-going oscillations around the distal ends of the dendrites (Fig. 10C). In response to this endogenous V_e field, the test neuron exhibits ~ 1.5 mV positive-going oscillations in V_m in the dendrites and smaller ~ 0.5 mV negative-going oscillations in the soma (Fig. 10B). Note that the test neuron does not receive any synaptic input in these simulations so these V_m changes are strictly due to ephaptic coupling.

The test neuron includes a SIZ in these simulations and V_e perturbs the SIZ's membrane potential (Fig 10E). In these and subsequent simulations, we compare three SIZ configurations illustrated in Fig. 10D: the “control” condition of no ephaptic coupling (black), ephaptic coupling and SIZ aligned with the soma (red),

and ephaptic coupling and SIZ aligned with a position $\sim 100 \mu\text{m}$ from the soma (cyan). If the SIZ is located near the soma, its membrane potential exhibits negative-going oscillations similar to V_m in the soma of the test neuron (compare cyan line in Fig. 10E to green line in Fig. 10B). If the SIZ is located away from the soma, its membrane potential exhibits positive-going oscillations similar to the response of the test neuron dendrite (compare red line in Fig. 10E and blue line in Fig. 10B). Note that in both cases the SIZ is connected via the same internal, axial resistance to the soma of the MSO neuron model; the SIZ position only determines the V_e that the SIZ “sees.”

These simulations reveal that V_e can increase or decrease the SIZ membrane potential depending on the position of the SIZ. Do ephaptic interactions alter spiking activity in MSO? We used conductance threshold as a measure of neuron excitability and found that ephaptic effects modulate the threshold curve depending on the location of the SIZ (Fig. 10F). If the SIZ is near the soma, we saw in Fig. 10E that V_e hyperpolarizes the SIZ membrane potential. This translates to an increase in threshold (diminished excitability) for all time differences tested. In contrast, the depolarizing effect of V_e on the SIZ located near the distal dendrites translates to a decrease in threshold, i.e. enhanced excitability.

The test neuron in these simulations received synaptic excitation in the form of excitatory (alpha function) synaptic events arriving on the two dendrites 15 ms after the start of the periodic input to the MSO population. The 15 ms delay ensured that any transient onset dynamics are avoided. We varied the difference in the timing of the two synaptic inputs to the test neuron (x -axis). A time difference of 0 ms represents coincident bilateral inputs to the test neuron. In this case the synaptic event times in the test neuron match the onset of one cycle of the rectified sine wave conductance input to the MSO population. Time differences larger than 0 ms (positive values on the x -axis of Fig. 10F) represent bilateral inputs to the test neuron that are not coincident. The synaptic event on one dendrite arrives earlier than the onset of the rectified sine wave input to the MSO population and the other synaptic event trails the onset of the rectified sine wave.

Conductance threshold is the smallest peak conductance needed to generate a spike in the SIZ. In the absence of ephaptic effects, thresholds increase with sub-millisecond increases in synaptic time difference (black line in Fig. 10F). This is confirmation that the model neuron, like MSO neurons, act as a coincidence detector. For the time differences tested in these simulations, ephaptic interactions decrease spike threshold by approximately $\sim 10\%$ for off-center SIZ and increase threshold by $\sim 10\%$ for centered SIZ.

Ephaptic coupling can entrain MSO spike timing: The small changes in spike threshold measured above can result in changes in spike timing. Specifically, we observed that periodic V_e can entrain a spontaneously firing neuron (Fig. 11A). In these simulations, we provided the test neuron with a random train of excitatory synaptic events that caused the test neuron to fire spontaneously at a rate of 20 spikes per second in the absence of ephaptic coupling (black line). Firing rate is presented as the cycle histogram of the test neuron’s response. In the absence of

ephaptic interactions, there is no 200 Hz “rhythm” to entrain spike times, thus the cycle histogram is flat for the spontaneously firing neuron.

When we repeated the simulation in the presence of a 200 Hz endogenously-generated V_e , we found that ephaptic interactions temporally modulate spike timing. Consistent with our previous results, the effect of V_e differs depending on the location of the SIZ. For the centered SIZ (cyan line), ephaptic coupling reduces firing rates during the first half of the 5 ms cycle and increases firing rates during the second half of the cycle. The cumulative effect of this V_e -induced firing rate modulation is a decrease of ~ 1.4 spike per second. For the off-center SIZ, the effect is opposite (red line). Ephaptic coupling increases firing rates during the first half of the 5 ms period and decreases firing rates thereafter. The cumulative change is an extra ~ 1.7 spikes per second due to ephaptic coupling. Simulations that include ephaptic coupling and the off-center SIZ produce spikes that are more likely to occur in phase with the periodic input to the MSO population. Thus the ephaptic interaction can entrain the test neuron’s spikes, even though inputs to the test neuron are random and do not have a periodic structure.

To construct the input to each dendrite of the test neuron, we combined 10 independent realizations of a homogeneous Poisson process (100 Hz event rate) to generate 10 independent input trains of “spike times.” We then convolved these event times with an alpha function (0.2 ms time constant, see Eq. 20). Each “unitary” synaptic event had a peak conductance of 10 mS/cm² that increases the SIZ membrane potential by 4.5mV. The simultaneous arrival of four such events (two per dendrite) can evoke a spike in the SIZ as can the arrival of six such events on a single dendrite.

Ephaptic coupling influences MSO coincidence detection: As a final test of ephaptic interactions, we simulated the standard measure of MSO neuron’s tuning to sound location: time difference tuning curves (Fig. 11B). Inputs to the test neuron were constructed from inhomogeneous Poisson processes with the Poisson rate given by a 200 Hz rectified sine wave. The inputs to the test neuron and MSO population have the same timing relative to one another, but there can be a time difference between the inputs on opposite dendrite. The x-axis reports the time difference in the bilateral inputs, a time difference of 0 ms indicates inputs that are identical on the two dendrites. A non-zero time difference indicates a phase difference between the sine wave rate functions.

The test neuron responds maximally when the Poisson rate functions are in phase on the two dendrites (0 ms time difference). This is another indication that the MSO model neuron acts as a coincidence detector with submillisecond temporal precision. In the absence of ephaptic coupling, the maximal firing rate is 166 Hz and decreases for larger time differences (black line in Fig. 11B). When ephaptic coupling is included, the effect on time difference tuning depends on the SIZ location in a manner consistent with our previous tests. Ephaptic coupling and the centered SIZ combine to have an “inhibitory” effect that reduces firing rates (cyan line, firing rate at 0 ms time difference is 159 spikes per second). Ephaptic coupling and the off-center SIZ combine to have an “excitatory” effect that increases firing rates (red line, firing rate at 0 ms time difference is 174 spikes per second). Taken together, the results in Fig. 11 illustrate that the nonlinear nature of spike generation can

amplify small changes in membrane potential. Millivolt-scale ephaptic interactions can plausibly alter spike activity in neurons and circuits.

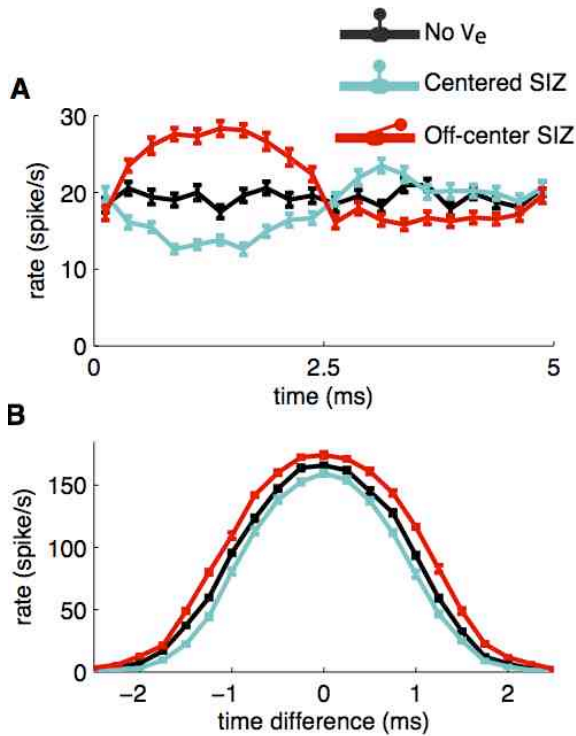


Figure 11: Ephaptic effects on spike timing and coincidence detection. **(A)** Cycle histogram of test neuron response to bilateral trains of excitatory synaptic events. Event times of input trains are generated from independent homogeneous Poisson processes (10 trains per dendrite). Event rate for the underlying Poisson process is 100 events per second. Average firing rates calculated in 0.25 ms bins from 50 simulations of responses to 10 second long input trains. Error bars are standard error of the mean. **(B)** Time difference tuning curves for test neuron's response to bilateral trains of excitatory synaptic events. Event times of input trains are generated from independent inhomogeneous Poisson processes (10 trains per dendrite). Event rate for the underlying Poisson process is a 200 Hz rectified sine wave with an average event rate of 100 events per second. The timing difference of the rectified sine wave Poisson rates is shown on the x-axis with 0 ms time difference representing rate functions to both dendrites that are in phase relative to one another and relative to the input to the MSO population. Firing rates were computed from responses to 10 second long inputs. Mean and standard error of the mean (error bars) were obtained by dividing these responses into 10 segments and counting spikes in each one second long subintervals. In all simulations (A and B): Unitary events synaptic events are alpha function conductances with 0.2 ms time constant and 10 mS/cm² maximal conductance, model configurations and color code are same as in Fig. 10D. Input to MSO population (generators of V_e) is 200Hz rectified sine wave excitation (20 mS/cm² maximal conductance) with same bilateral time differences as input to test neuron.

DISCUSSION

Summary of main findings

Neural activity generates transmembrane currents that, in turn, generate spatiotemporal patterns of extracellular voltage. Nearby neurons are embedded in this shared, endogenously-generated V_e . V_e can provide, therefore, a channel for non-synaptic communication between neurons. Following the insightful early work of Arvanitaki (1942), we refer to this phenomenon as *ephaptic* coupling.

We have developed and analyzed a model of ephaptic interactions in an idealized one-dimensional setting (computer code available on ModelDB). We considered a population of identical passive cables as an idealized model of uniform, unbranched neurons receiving identical inputs. We illustrated how ephaptic coupling in this system can be described with an extension of cable theory that accounts for dynamical coupling between one-dimensional intra- and extracellular domains. We identified the strength of extracellular coupling by introducing a new dimensionless parameter $\kappa = \rho\delta/(1-\delta)$, where ρ is the ratio of volume resistivities R_e/R_i and δ is the packing density of neurons and offered plausible estimates for κ .

We found that the idealized neuron population could generate millivolt-scale V_e and this V_e could induce millivolt-scale perturbations in the membrane potential of an additional “test” neuron embedded in the endogenously-generated V_e . We varied the spatial profile of V_e by varying the localized stimulus input site and found that the amplitude of the V_m perturbation remained relatively constant (Fig. 3). We also found that electrotonically compact cables (large space constant λ) experience larger changes in their V_m due to coupling to V_e than electrotonically long cables (small space constant λ) (Fig. 4) and compact cables generate larger amplitude V_e responses (Fig. 5). For sinusoidal inputs, ephaptic effects at low frequencies were similar to steady state responses (Fig. 6) and attenuated in response to higher frequency inputs due to the low-pass dynamics imposed by the passive cable (Fig. 7).

We applied the same one-dimensional idealization to model V_e generated by simultaneously activated and spatially aligned neurons in the medial superior olive (MSO) of the auditory brainstem. These neurons have a relatively simple structure: a soma and two dendrites extending away from the soma with minimal branching. The qualitative features of ephaptic coupling in the passive cable model and this more biophysically-detailed model were broadly similar. Our simulations used physiologically plausible parameters and fast synaptic conductances and demonstrated that MSO neurons can generate millivolt-scale V_e responses that induce millivolt-scale perturbations in a “test” MSO neuron (Figs. 8 and 9).

The MSO is a critical early stage of binaural processing and it can extract information regarding the location of sound sources in the environment. MSO neurons receive inputs arriving from both ears and they are sensitive to submillisecond timing differences in these inputs. We were particularly interested, therefore, to determine whether ephaptic effects and their instantaneous nature can alter the precise coincidence detection computation performed by MSO neurons. We tested ephaptic effects on MSO spiking by adding a spike initiation zone (SIZ) to a test neuron embedded in the endogenously-generated (simulated) V_e . We found that millivolt-scale ephaptic effects can change the spike output of MSO neurons. The location of the SIZ in the spatially-distributed V_e is critical. We compared two configurations: a “centered” SIZ aligned with the soma and an “off-center” SIZ located $\sim 100 \mu\text{m}$ away from the soma (see schematic in Fig. 10D). V_e can act in an “excitatory” or “inhibitory” manner depending on the SIZ position. In particular, for an SIZ located away from the soma, V_e produced by in phase bilateral inputs to the MSO population depolarized V_m in the SIZ (Fig. 10E), decreased thresholds for spike

generation (Fig. 10F), entrained spike times to the ongoing V_e oscillation (Fig. 11A), and increased the gain of a simulated time-difference tuning curve (Fig. 11B). If the SIZ is aligned with the soma, V_e has opposite effects and suppresses spiking activity.

Relation to previous work

Our model relies on the idealization that neural dynamics in the presence of ephaptic interactions can be described by coupling a one-dimensional intracellular domain (cable core conductor) to a one-dimensional extracellular volume conductor. We arrived at this simplified geometry by taking a mean-field view of a large population of identical cables organized in parallel to one another and receiving identical inputs. This construction may appear overly simplistic, but it is inspired by pioneering studies of endogenously-generated V_e (Rall and Shepherd 1968, Nicholson and Llinás 1971) and we have recently used a similar formulation to study *in vivo* V_e in the auditory brainstem of cats (Goldwyn et al 2014). Alternative methods have been formulated that include more realistic neural morphologies and extracellular volume conductors (Malik 2011, Agudelo-Toro and Neef 2013), but these methods have the drawback of requiring substantial computing resources. In addition, the one-dimensional intracellular and extracellular domains facilitate visualization and analyses of simulation results. The validity of the one-dimensional volume conductor model could be evaluated in future studies with these more sophisticated computational methods.

A number of our observations concur with earlier studies of V_e effects on passive cables. Rall (1977) pointed out that coupling to V_e decreases the cable space constant from $\sqrt{r_m/r_i}$ to $\sqrt{r_m/(r_i + r_e)}$. Recent studies have pointed out that increasing the space constant of a cable (larger r_m and/or smaller r_i) increases the effect of V_e on V_m (Anastassiou et al 2010, Frölich and McCormick 2010). We identified the upper bound of the ephaptic effect for steady state responses to constant localized input as $-V_e + \frac{1}{L} \int_0^L V_e dX$ (see Fig. 4B).

We showed that a periodic V_e can alter spike timing in MSO model neurons (Fig. 11A). Recent studies have reported similar results *in vitro* and in simulation studies (Frölich and McCormick 2010, Anastassiou et al 2011). Specifically, these studies applied periodic extracellular fields to cortical slice preparations and demonstrated that spike timing can be entrained to the “rhythm” of ongoing, periodic V_e . A novel finding in our study is that the location of the SIZ matters when considering the effect of V_e on spike timing. V_e can indeed entrain neurons and enhance spike synchrony (Fig. 11A, off-center SIZ). It is also possible, however, that the SIZ could be located in a region of extracellular space where V_e decreases the SIZ membrane potential and suppresses spike output (Fig. 11A, centered SIZ). This could reduce spike time synchrony across a population. We did not consider the contribution of spikes to V_e because they are not prominent in MSO field potentials. A recent modeling study of layer V pyramidal cells has demonstrated that V_e generated by spikes is capable of altering spike timing in simulations (Stacey et al. 2015).

Implications for functional ephaptic coupling

Applied extracellular voltage affects cell-level and circuit-level neural activity; this is the principle by which neural prostheses such as cochlear implants, retinal implants, and deep brain stimulation operate. We are concerned with a complementary question: does endogenously-generated V_e act as a form of non-synaptic, global coupling to alter neural dynamics?

Studies in diverse neural structures have identified ephaptic coupling as a means of fast, non-synaptic inhibition (teleost Mauthner-cell system in goldfish, Weiss et al. 2008; olfactory receptor neurons in insects, Su et al. 2012; pinceau structure surrounding axon initial segment of cerebellar Purkinje cell, Blot and Barbour 2014). Figure 2 illustrates how ephaptic coupling could operate in an inhibitory manner in a bundle of neurons. Excitatory inputs arriving near the terminal of a neural structure (a distal dendrite site, e.g.) hyperpolarize the opposite end (e.g., soma and initial segment) of neighboring neural structures through the ephaptic interaction.

Figure 2 also illustrates that ephaptic interactions could promote local excitation. Excitatory inputs arriving near the end, say proximal end, of a neural structure locally depolarize the proximal end of nearby neurons through the ephaptic interaction. This local depolarization could be enhanced further in dendritic bundles with regenerative currents and provide a non-synaptic mechanism for simultaneously exciting dendrites in a local population. Bokil et al. (2001) demonstrated this type of “excitatory” ephaptic coupling in simulations of a bundle of axons. They found, using a mean field formulation similar to ours, that spikes in an axon can promote spike generation and spike time synchrony in nearby axons. The capacity for V_e to depolarize nearby neurons via an “excitatory” ephaptic effect has also been proposed as a mechanism for epileptogenesis in the hippocampus (Traub et al. 1985, Zhang et al. 2014).

Our MSO simulations that included a spike initiation zone (SIZ) in the test neuron demonstrated that even small ephaptic effects (millivolt-scale) can alter spiking activity (Fig. 11). The nonlinear nature of spike generation can amplify ephaptic coupling (see also: Radman et al 2007, Anastassiou et al. 2011). We found that the anatomy of the spike generator matters for neurons embedded in a spatially-varying V_e . Ephaptic coupling can have opposing “excitatory” or “inhibitory” effects depending on the orientation of axons and the site of spike generation. We are not aware of a comprehensive study of axon anatomy in the MSO. This makes it difficult for us to make specific predictions regarding possible functional effects of ephaptic coupling in MSO. A recent study has examined spike generation in MSO axons and the anatomy of the MSO axon initial segment (Lehnert et al 2014). Further work in this direction would contribute to our understanding of ephaptic coupling the MSO. Auditory brainstem neurons in the chick exhibit plasticity in the length of the axon initial segment (specifically, the distribution of Na channels) (Kuba et al 2010). This raises the possibility that ephaptic effects could be modulated over time.

Our cable theory-based study of ephaptic interactions among passive cables has informed our understanding of ephaptic interactions in MSO neurons. We view the MSO as a useful “model system” to explore these effects because V_e is large and

sound-evoked *in vivo*, spatio-temporal features of the V_e response can be modeled with the mean-field approximation and a one-dimensional volume conductor (Goldwyn et al 2014), and MSO neurons perform a known computation. That computation – coincidence detection of binaural inputs – is typically studied by recording (or simulating) time-difference tuning curves analogous to Fig. 11B. We found that ephaptic coupling could increase or decrease the gain of the time-difference tuning curve, depending on the location of the spike generator (but the tuning curve width was not changed appreciably). Our simulations establish a “proof of principle” that ephaptic interactions can alter binaural processing in the MSO. We cannot yet identify a functional role for ephaptic coupling in the MSO, but this remains an intriguing avenue for future research.

Acknowledgements

Large-scale simulations were supported by computing resources at the New York University High Performance Computing Center and an allocation of computing time from the Ohio Supercomputer Center.

Grants

This research has been supported by funding from the National Institute on Deafness and Other Communication Disorders: F32 DC012978 (JHG) and R01 DC008543 (JR).

Disclosures

The authors declare that they have no conflict of interest, financial or otherwise, pertaining to this work.

References

- Agudelo-Toro A, Neef, A.** Computationally efficient simulation of electrical activity at cell membranes interacting with self-generated and externally imposed electric fields. *J Neural Eng* 10: 026019, 2013.
- Anastassiou CA, Montgomery SM, Barahona M, Buzsáki G, Koch C.** The effect of spatially inhomogeneous extracellular electric fields on neurons. *J Neurosci* 30: 1925-1936, 2010.
- Anastassiou CA, Perin R, Markram H, Koch, C.** Ephaptic coupling of cortical neurons. *Nat Neurosci* 14: 217-223, 2011.
- Arvanitaki A.** Effects evoked in an axon by the activity of a contiguous one. *J Neurophysiol* 5: 89-108, 1942.
- Ashida G, Carr CE.** Sound localization: Jeffress and beyond. *Curr Opin Neurobiol* 21: 745-751, 2011.
- Biedenbach MA, Freeman WJ.** Click-evoked potential map from the superior olivary nucleus. *Am J Phys* 206: 1408-1414, 1964.
- Blot A, Barbour B.** Ultra-rapid axon-axon ephaptic inhibition of cerebellar Purkinje cells by the pinceau. *Nat Neurosci* 17: 289-295, 2014.
- Bokil H, Laaris N, Blinder K, Ennis M, Keller A.** Ephaptic interactions in the mammalian olfactory system. *J Neurosci* 21: RC 173, 2001.
- Buzsáki G, Anastassiou CA, Koch, C.** The origin of extracellular fields and currents — EEG, ECoG, LFP and spikes. *Nat Rev Neurosci* 13: 407-420, 2012.
- Clark GM, Dunlop CW.** Field potentials in the cat medial superior olivary nucleus. *Exp Neurol* 20: 31-42, 1968.
- Couchman K, Grothe B, Felmy F.** Functional localization of neurotransmitter receptors and synaptic inputs to mature neurons of the medial superior olive. *J Neurophysiol* 107: 1186-1198, 2012.
- Fischl MJ, Combs TD, Klug A, Grothe B, Burger RM.** Modulation of synaptic input by GABAB receptors improves coincidence detection for computation of sound location. *J Physiol* 590(Pt 13): 3047-3066, 2012.
- Franken TP, Roberts MT, Wei L, Golding NL, Joris PX.** *In vivo* coincidence detection in mammalian sound localization generates phase delays. *Nat Neurosci* 18: 444-452, 2015.
- Frölich F, McCormick DA.** Endogenous electric fields may guide neocortical network activity. *Neuron* 67: 129-143, 2010.
- Galambos R, Schwartzkopff J, Rupert, A.** Microelectrode study of superior olivary nuclei. *Am J Phys* 197: 527-536, 1959.
- Geddes LA, Baker LE.** The specific resistance of biological material – A compendium of data for the biomedical engineer and physiologist. *Med Biol Eng* 5: 271-293, 1967.
- Golding NL, Oertel D.** Synaptic integration in dendrites: exceptional need for speed. *J Physiol* 590: 5563-5569, 2012.
- Goldwyn JH, Mc Laughlin M, Verschooten E, Joris PX, Rinzel J.** A model of the medial superior olive explains spatiotemporal features of the local field potentials. *J Neurosci* 34: 11705-11722, 2014.

- Graham RL, Lubachevsky BD, Nurmela KJ, Östergård, PRJ.** *Discrete Math* 181: 139-154, 1998.
- Grothe B, Pecka M, McAlpine D.** Mechanisms of sound localization in mammals. *Physiol Rev* 90: 983-1012, 2010.
- Grothe B, Sanes DH.** Bilateral inhibition by glycinergic afferents in the medial superior olive. *J Neurophysiol* 69: 1192–1196, 1993.
- Grothe B, Sanes DH.** Synaptic inhibition influences the temporal coding properties of medial superior olivary neurons: an in vitro study. *J Neurosci* 14: 1701–1709, 1994.
- Hindmarsh AC, Brown PN, Grant KE, Lee SL, Serban R, Shumaker DE, Woodward CS.** SUNDIALS: SUite of Nonlinear and Differential/ALgebraic Equation Solvers. *ACM Trans Math Software* 31: 363–396, 2005.
- Holt GR, Koch C.** Electrical interactions via the extracellular potential near cell bodies. *J Comput Neurosci* 6: 169–184, 1999.
- Huguet G, Meng X, Rinzel J.** Phasic firing, by divisive or subtractive feedback, can perform coincidence detection – but how well? Program 540.26/D57. *Society for Neuroscience*, 2012.
- Koch C.** *Biophysics of Computation: Information Processing in Single Neurons*. New York: Oxford University Press, 1998, p. 47.
- Jercog PE, Svirskis G, Kotak VC, Sanes DH, Rinzel J.** Asymmetric excitatory synaptic dynamics underlie interaural time difference processing in the auditory system. *PLoS Biol* 8: e1000406, 2010.
- Joris PX, Carney LH, Smith PH, Yin TC.** Enhancement of neural synchronization in the anteroventral cochlear nucleus. I. Responses to tones at the characteristic frequency. *J Neurophysiol* 71: 1022-1036, 1994.
- Katz B, Schmitt OH.** Electric interaction between two adjacent nerve fibers. *J Physiol* 97: 471-488, 1940.
- Klee M, Rall W.** Computed potentials of cortically arranged populations of neurons. *J Neurophysiol* 40: 647-666, 1977.
- Khurana S, Remme MWH, Rinzel J, Golding NL.** Dynamic interaction of I_h and I_{K-LVA} during trains of synaptic potentials in principal neurons of the medial superior olive. *J Neurosci* 31: 8936-8947, 2011.
- Kuba H, Oichi Y, Ohmori, H.** Presynaptic activity regulates Na^+ channel distribution at the axon initial segment. *Nature* 465: 1075-1078, 2010.
- Lehnert S, Ford MC, Alexandrova O, Hellmundt F, Felmy F, Grothe B, Leibold C.** Action potential generation in an anatomically constrained model of medial superior olive axons. *J Neurosci* 34: 5370–5384.
- Lindén H, Tetzlaff T, Potjans TC, Pettersen KH, Grün S, Diesmann M, Einevoll GT.** Modeling the spatial reach of the LFP. *Neuron* 72: 859-872, 2011.
- Lorente de Nò R.** Action potential of the motoneurons of the hypoglossus nucleus. *J Cell Comp Physiol* 29: 207-287, 1947.
- Lucht W, Strehmel K, Eichler-Liebenow C.** *Linear partial differential algebraic equations, Part I: Indexes, consistent boundary/initial conditions* (Report 17). Fachbereich Mathematik und Informatik, Martin-Luther-Universität, Halle, 1997.

- Lucht W, Strehmel K, Eichler-Liebenow C.** *Linear partial differential algebraic equations, Part II: Numerical solution* (Report 18). Fachbereich Mathematik und Informatik, Martin-Luther-Universität, Halle, 1997.
- Malik, NA.** *Frequency-dependent response of neurons to oscillating electric fields.* (PhD dissertation). University of Warwick, 2011.
- Mathews PJ, Jercog PE, Rinzel J, Scott LL, Golding NL.** Control of submillisecond synaptic timing in binaural coincidence detectors by Kv1 channels. *Nat Neurosci* 13: 601–609, 2010.
- Mc Laughlin M, Verschooten E, Joris PX.** Oscillatory dipoles as a source of phase shifts in field potentials in the mammalian auditory brainstem. *J Neurosci* 30: 13472–13487, 2010.
- Moushegian G, Rupert A, Whitcomb MA.** Medial superior-olivary-unit response patterns to monaural and binaural clicks. *J Acoust Soc Amer* 36: 196-202, 1964.
- Myoga MH, Lehnert S, Leibold C, Felmy F, Grothe B.** Glycinergic inhibition tunes coincidence detection in the auditory brainstem. *Nat Commun* 5: 3790, 2014.
- Nicholson C, Llinás R.** Field potentials in the alligator cerebellum and theory of their relationship to Purkinje cell dendritic spikes. *J Neurophysiol* 34: 509-531, 1971.
- Radman T, Su Y, An JH, Parra LC, Biksom M.** Spike timing amplifies the effect of electric fields on neurons: Implications for endogenous field effects. *J Neurosci* 27: 3030–3036, 2007.
- Rall W.** Core conductor theory and cable properties of neurons. In: *Handbook of Physiology. Cellular biology of Neurons.* Bethesda, MD: Am. Physiol. Soc., 1977, p. 39-97. .
- Rall W, Shepherd GM.** Theoretical reconstruction of field potentials and dendrodendritic synaptic interactions in olfactory bulb. *J Neurophysiol* 31: 884-915, 1968.
- Ramón F, Moore JW.** Ephaptic transmission in squid giant axons. *Am J Physiol* 234: C162–C169, 1978.
- Rattay F.** Analysis of Models for External Stimulation of Axons. *IEEE Trans Biomed Eng* 33: 974–977, 1986.
- Rattay F.** The basic mechanism for the electrical stimulation of the nervous system. *Neuroscience* 89: 335–346, 1999.
- Rautenberg PL, Grothe B, Felmy F.** Quantification of the three-dimensional morphology of coincidence detector neurons in the medial superior olive of gerbils during late postnatal development. *J Comp Neurol* 517: 385-396, 2009.
- Reimann MW, Anastassiou CA, Perin R, Hill SL, Markram H, Koch C.** A biophysically detailed model of neocortical local field potentials predicts the critical role of active membrane currents. *Neuron* 79: 375-390, 2013.
- Rothman JS, Manis PB.** The roles potassium currents play in regulating the electrical activity of ventral cochlear nucleus neurons. *J Neurophysiol* 89: 3097–3113, 2003.
- Scott LL, Hage TA, Golding NL.** Weak action potential backpropagation is associated with high-frequency axonal firing capability in principal neurons of the gerbil medial superior olive. *J Physiol* 583: 647–661, 2007.

- Schwartz IR.** Dendritic arrangements in the cat medial superior olive. *Neuroscience* 2: 81–101, 1977.
- Segev I, Burke, RE.** Compartmental models of complex neurons. In: *Methods in neuronal modeling: From ions to networks*, edited by Koch C and Segev I. Cambridge, MA: MIT Press, 1998.
- Stacey RG, Hilbert L, Quail T.** Computational study of synchrony in fields and microclusters of ephaptically coupled neurons. *J Neurophysiol* 113: 3229-3241, 2015.
- Strumwasser F, Rosenthal S.** Prolonged and patterned direct extracellular stimulation of single neurons. *Am J Physiol* 198: 405–413, 1960.
- Su C-Y, Menuz K, Reisert J, Carlson, JR.** Non-synaptic inhibition between grouped neurons in an olfactory circuit. *Nature* 492: 66–71, 2012.
- Traub RD, Dudek FE, Taylor CP, Knowles WD.** Simulation of hippocampal afterdischarges synchronized by electrical interactions. *Neuroscience* 14: 1033-1038, 1985.
- Tsuchitani C, Boudreau JC.** Wave activity in the superior olivary complex of the cat. *J Neurophysiol* 27: 814-827, 1964.
- Tuckwell HC.** *Introduction to Theoretical Neurobiology: Volume 1, Linear Cable Theory and Dendritic Structure*. New York: Cambridge University Press, 1988, p. 130.
- van der Heijden M, Lorteije JAM, Plauska A, Roberts MT, Golding NL, Borst JGG.** Directional hearing by linear summation of binaural inputs at the medial superior olive. *Neuron* 78: 936 –948, 2013.
- Weiss SA, Preuss T, Faber DS.** A role of electrical inhibition in sensorimotor integration. *Proc Natl Acad Sci USA* 105: 18047–18052, 2008.
- Weisstein, EW.** Circle packing [Online]. Wolfram MathWorld. <http://mathworld.wolfram.com/CirclePacking.html> [3 March 2015].
- Yin TCT, Chan JCK.** Interaural time sensitivity in medial superior olive of cat. *J Neurophysiol* 64: 465–488, 1990.
- Zhang M, Ladas TP, Qui C, Shivacharan RS, Gonzales-Reyes LE, Durand DM.** Propagation of epileptiform activity can be independent of synaptic transmission, gap junctions, or diffusion and is consistent with electrical field transmission. *J Neurosci* 34: 1409–1419, 2014.